Molecular Cell

Article

Structural basis for OAS2 regulation and its antiviral function

Graphical abstract

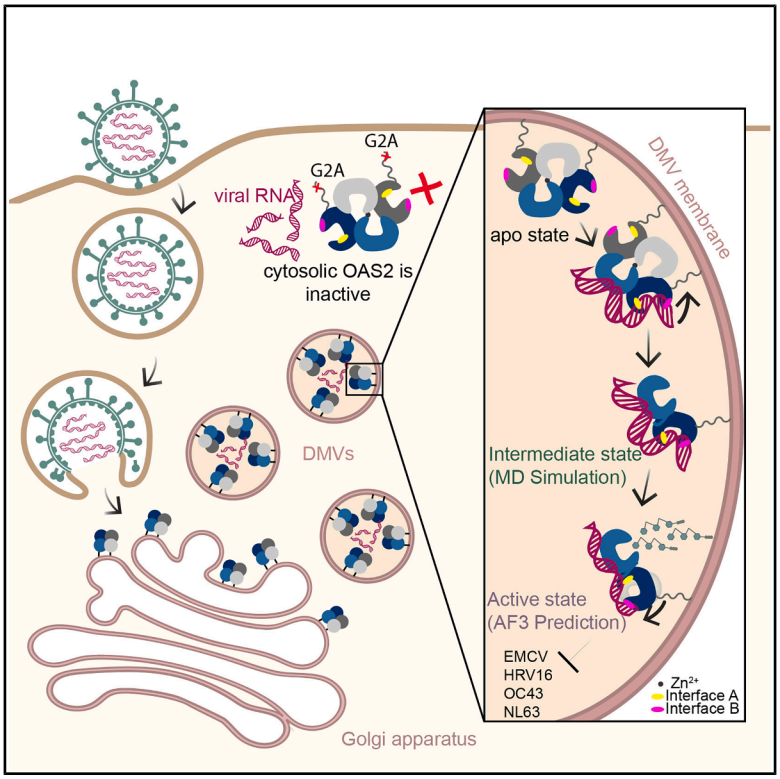

Highlights

- Cryo-EM structure reveals auto-inhibited zinc-mediated OAS2 dimer
- Non-canonical dsRNA-binding site in domain DI controls RNA length specificity
- OAS2 Golgi localization is essential for dsRNA sensing and antiviral response
- Heterozygous LOF OAS2 F524L mutation is associated with pediatric autoimmunity

Authors

Veronika Merold, Indra Bekere, Stefanie Kretschmer, ..., Konstantin M. J. Sparrer, Min Ae Lee-Kirsch, Carina C. de Oliveira Mann

Correspondence

carina.mann@tum.de

In brief

Merold and Bekere et al. reveal that OAS2 exists as a zinc-mediated dimer in an autoinhibited state, preventing autoreactivity to short RNAs. Dimer-to-monomer transition, dsRNA binding to a non-canonical interface, and targeting to the Golgi by myristoylation are necessary for OAS2 activation and restriction of viruses that form double membrane vesicles.

Merold et al., 2025, Molecular Cell *85*, 1–18
June 5, 2025 © 2025 The Authors. Published by Elsevier Inc.
https://doi.org/10.1016/j.molcel.2025.05.001

CellPress

Please cite this article in press as: Merold et al., Structural basis for OAS2 regulation and its antiviral function, Molecular Cell (2025), https://doi.org/10.1016/j.molcel.2025.05.001

Molecular Cell

CellPress
OPEN ACCESS

Article

Structural basis for OAS2 regulation and its antiviral function

Veronika Merold,[1,16] Indra Bekere,[1,16] Stefanie Kretschmer,[2] Adrian F. Schnell,[3] Dorota Kmiec,[4] Rinu Sivarajan,[4] Katja Lammens,[5] Rou Liu,[2] Julia Mergner,[6] Julia Teppert,[7] Maximilian Hirschenberger,[4] Alexander Henrici,[8] Sarah Hammes,[1] Kathrin Buder,[9] Marcus Weitz,[9] Karl Hackmann,[10] Lars M. Koenig,[7] Andreas Pichlmair,[8,11,12] Nadine Schwierz,[3] Konstantin M.J. Sparrer,[4,13] Min Ae Lee-Kirsch,[2,14,15] and Carina C. de Oliveira Mann[1,17,*]

[1]Department of Bioscience, TUM School of Natural Sciences, Technical University of Munich, Garching 85748, Germany
[2]Department of Pediatrics, Medizinische Fakultät Carl Gustav Carus, Technische Universität Dresden, Dresden 01307, Germany
[3]Institute of Physics, University of Augsburg, Augsburg 86159, Germany
[4]Institute of Molecular Virology, Ulm University Medical Center, Ulm 89081, Germany
[5]Gene Center and Department of Biochemistry, Ludwig-Maximilians-Universität München, Munich 81377, Germany
[6]Bavarian Center for Biomolecular Mass Spectrometry at Klinikum Rechts der Isar, School of Medicine and Health, Technical University of Munich, Munich 81675, Germany
[7]Division of Clinical Pharmacology, University Hospital, Ludwig-Maximilians-Universität München, Munich 80337, Germany
[8]School of Medicine, Institute of Virology, Technical University of Munich, Munich 81675, Germany
[9]University Hospital Tuebingen, University Children's Hospital, Department of General Pediatrics and Hematology/Oncology, Tuebingen 72076, Germany
[10]Institute for Clinical Genetics, University Hospital Carl Gustav Carus at TUD Dresden University of Technology, Dresden 01307, Germany
[11]Helmholtz Center Munich, Systems Virology, Neuherberg 85764, Germany
[12]German Center for Infection Research, Partner site Munich, Munich 81675, Germany
[13]German Center for Neurodegenerative Diseases, Ulm 89081, Germany
[14]University Center for Rare Diseases, Medizinische Fakultät Carl Gustav Carus, Technische Universität Dresden, Dresden 01307, Germany
[15]German Center for Child and Adolescent Health, partner site Leipzig/Dresden, Dresden 01307, Germany
[16]These authors contributed equally
[17]Lead contact
*Correspondence: carina.mann@tum.de
https://doi.org/10.1016/j.molcel.2025.05.001

SUMMARY

Oligoadenylate synthetase (OAS) proteins are immune sensors for double-stranded RNA and are critical for restricting viruses. OAS2 comprises two OAS domains, only one of which can synthesize 2′–5′-oligoadenylates for RNase L activation. Existing structures of OAS1 provide a model for enzyme activation, but they do not explain how multiple OAS domains discriminate RNA length. Here, we discover that human OAS2 exists in an auto-inhibited state as a zinc-mediated dimer and present a mechanism for RNA length discrimination: the catalytically deficient domain acts as a molecular ruler that prevents autoreactivity to short RNAs. We demonstrate that dimerization and myristoylation localize OAS2 to Golgi membranes and that this is required for OAS2 activation and the restriction of viruses that exploit the endomembrane system for replication, e.g., coronaviruses. Finally, our results highlight the non-redundant role of OAS proteins and emphasize the clinical relevance of OAS2 by identifying a patient with a loss-of-function mutation associated with autoimmune disease.

INTRODUCTION

Double-stranded RNA (dsRNA) is one of the most relevant signatures of viral replication sensed by the immune system. dsRNA is detected in the cytoplasm through different classes of immune receptors and restriction factors. 2′–5′ oligoadenylate synthetase (OAS) proteins are interferon-induced antiviral enzymes that require binding to dsRNA for activation.[1–9] As part of the nucleotidyltransferase (NTase) protein family and structurally related to the dsDNA receptor cyclic GMP-AMP synthase (cGAS), OAS proteins synthesize unique second messengers that feature 2′–5′ phosphodiester bonds by oligomerizing ATP into 2′–5′-oligoadenylates (2′–5′OAs).[4,9–17] 2′–5′OAs, in turn, bind and activate latent RNase L, which degrades both viral and cellular single-stranded RNA (ssRNA), resulting in translational arrest and viral restriction.[18–25] A dysregulation of OAS1 function has been implicated in various autoinflammatory conditions and increased risk of severe outcomes in COVID-19.[26–33]

This is an open access article under the CC BY license (http://creativecommons.org/licenses/by/4.0/).

Please cite this article in press as: Merold et al., Structural basis for OAS2 regulation and its antiviral function, Molecular Cell (2025), https://doi.org/10.1016/j.molcel.2025.05.001

Recently, hypomorphic loss-of-function variants in OAS1 and OAS2 have been connected to multisystem inflammatory syndrome in children (MIS-C) following SARS-CoV-2 infection.[34]

Humans express three catalytically active OAS proteins, OAS1, OAS2, and OAS3. OAS1 consists of a single OAS domain of the polymerase beta (pol-β)-like NTase fold that harbors the catalytic triad required for 2'–5'OA synthesis.[35–41] OAS2 and OAS3 contain two and three OAS domains, respectively, which have evolved through gene duplication events.[5,42,43] Only one OAS domain in each OAS protein has retained the catalytic triad in the active site, raising the question of the role played by the catalytically inactive pseudo-OAS domains.[44] Despite not having catalytic activity, these pseudo-OAS domains were shown to be required for activation of OAS2 and OAS3.[45–48] A current model suggests that OAS proteins have different minimal RNA length requirements for activation, similar to cGAS.[49] OAS1 is activated by short >18-bp-long dsRNA, OAS2 by >35-bp-medium-long dsRNA, and OAS3 by >50-bp-long dsRNA. Although the structural mechanism for OAS1 activation by short dsRNA is well described, a major limitation in our understanding of OAS protein function is the lack of structural information for multi-domain OAS proteins. All current structural and mechanistic information is therefore derived from crystal structures of isolated OAS domains such as OAS1 or OAS3 domain I (DI).[36–38,45] Thus, despite being among the first antiviral proteins discovered, the mechanism underlying the length-dependent activation of OAS proteins by dsRNA remains elusive. Importantly, in addition to different RNA ligands, the varied subcellular localization of OAS proteins has recently been demonstrated to contribute to their unique roles in virus restriction. Although OAS3 recognizes viruses that replicate in the cytosol, OAS1 p46 is targeted to the endomembrane system through prenylation to detect viral dsRNAs directly at their replication organelles.[15,29,30,50–53] Similarly, OAS2 is myristoylated at its N terminus.[16,54,55] However, the impact of subcellular targeting on its antiviral activity and specificity remains unclear. These unexplored questions regarding the functions of OAS proteins have resulted in a generalized understanding of their roles, often viewed solely through the lens of RNase L activation. We are now beginning to appreciate the non-redundant functions of OAS proteins in antiviral immunity. Here, we define an unexpected mechanism of OAS2 regulation that prevents OAS2 activation by short dsRNA and determine how subcellular localization of OAS2 defines its antiviral activity. In line with non-redundant functions of OAS proteins, complete loss of function of OAS2 is associated with severe autoimmune disease in a patient. Our results define a mechanism of OAS2 regulation that explains how OAS2 discriminates between RNA lengths and how association with Golgi membranes is required for OAS2 antiviral functions.

RESULTS

Structure of human OAS2 reveals dimerization via a zinc-binding site

OAS2 consists of two OAS domains: a catalytically deficient domain DI (residues 13–325) and a catalytically active domain DII (residues 345–686), which share their overall structural fold with limited sequence identity (42.9%) (Figures 1A and S1). We purified full-length OAS2 p71 to understand how multiple domains connected by a linker are regulated. During the purification of the OAS2 protein, gel filtration showed that OAS2 is a dimer, in contrast to monomeric OAS1 and OAS3 (Figures S2A and S2B). Oligomerization was already found to be important for OAS1 and OAS2.[15,46,48,56] To mechanistically understand how dimerization of OAS2 regulates its activation, we solved the structure of human OAS2 using cryoelectron microscopy (cryo-EM) to an overall resolution of 3.3 Å (Table 1, Figures S2C, S2D–S2G, and S2I). The OAS2 dimer has a bowl-shaped conformation with an interface of 3,441.9 Å^2 between the monomers, which are positioned in an antiparallel orientation to each other (Figures 1B, 1C, and 1D). This mode of dimerization traps OAS2 in an inactive conformation (Figures S2H and 1C). The active site is not aligned for catalysis, but the helical P-loop (residues 396–399) is formed in the absence of dsRNA, as has been reported for other NTase/OAS domain structures (Figure S2H).[37,45,57,58] This places DII within the OAS2 dimer in a hybrid conformation.

The OAS2 dimer is held together by an unexpected tetrahedral zinc coordination site in the middle of the hydrophobic dimerization interface (Figure 1C). Residues C652 and H654 of the catalytically active DII of each monomer coordinate the binding of a zinc atom. This DII-driven dimerization mechanism allows DII to remain inactive even in the absence of DI, explaining why previous attempts to activate the isolated DII domain *in vitro*, analogous to OAS1, have failed.[46,48] C652 and H654 are conserved in OAS2 but not in OAS1 and OAS3, revealing a dimerization mechanism unique to OAS2 (Figures 1E and S1). When comparing the AlphaFold3[59] prediction for the OAS2 dimer with the model of our structure, we observe large deviations (root-mean-square deviation [RMSD] = 1.01 nm). Even when provided Zn^{2+} as a ligand, the resulting AF3 prediction deviated from our OAS2 structure (RMSD = 0.68 nm) (Figures S2J and S2K).

Mutation of OAS2 C652S is sufficient to disrupt the dimer interface and to render OAS2 monomeric (Figures 1F and S2B). Given the inactive conformation of the catalytic site of the OAS2 dimer, we hypothesized that OAS2 must monomerize to be properly activated by its ligand dsRNA. To test this hypothesis, we compared the *in vitro* activity of the wild-type OAS2 with that of the OAS2 C652S. Our results show that the OAS2 C652S is significantly more active in the presence of dsRNA than the wild-type OAS2, providing evidence that monomerization of OAS2 is a previously unknown requirement that facilitates activation by dsRNA (Figure 1G). These results provide the structural framework for multiple OAS domains and reveal a mechanism by which dimerization via metal coordination keeps the protein in an auto-inhibited state, creating an unexpected level of regulation that controls 2′–5′OA synthesis.

RNA ligand requirements for the activation of OAS2 differ from those of OAS1 and OAS3

Research into how OAS proteins recognize RNA has concentrated on their ability to discriminate dsRNAs based on minimal length requirements.[60] OAS1 binds dsRNA to a positively charged groove opposite the active site with a footprint of

Please cite this article in press as: Merold et al., Structural basis for OAS2 regulation and its antiviral function, Molecular Cell (2025), https://doi.org/10.1016/j.molcel.2025.05.001

CellPress
OPEN ACCESS

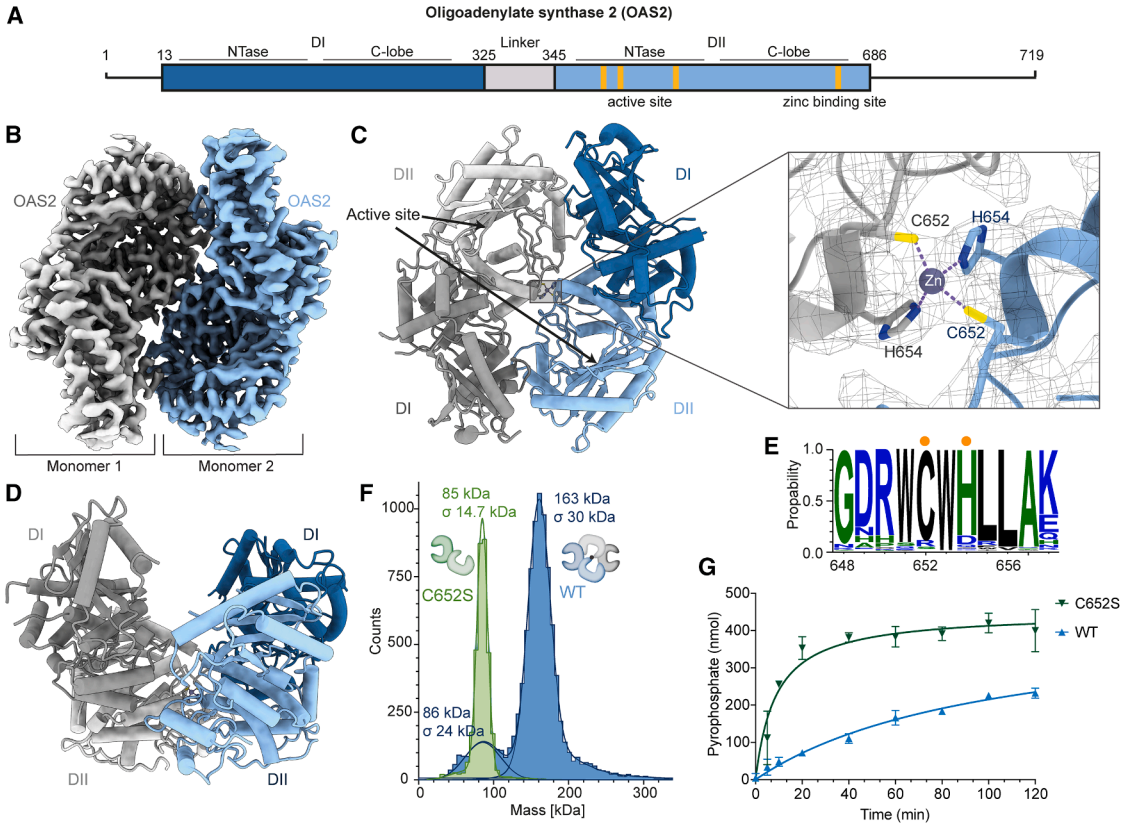

Figure 1. Structure of human OAS2 reveals dimerization via a zinc-binding site

(A) Domain organization of human OAS2.

(B) Cryo-EM reconstruction of OAS2 in 3.3 Å resolution. Two monomers are depicted in blue and gray, respectively.

(C) Atomic model of OAS2 dimer with close-up of Zn^{2+} coordination of DII C652 and H654 from each monomer (blue and gray). Inactive domain DI is shown in darker color, active domain DII in lighter color. Electron density is depicted as gray mesh.

(D) Side view of OAS2 dimer.

(E) Sequence logo of 210 species showing conservation of C652 and H654.

(F) Mass photometer analysis of monomeric OAS2 C652S (green) compared with dimeric OAS2 wild type (blue).

(G) *In vitro* chromogenic activity assay of 100 nM OAS2 wild type (blue) and C652S (green) with 82-bp-long dsRNA (100 nM) (mean ± SD of $n = 3$).

See also Figures S1 and S2.

17 bp and a preference for a consensus sequence.[37,38,49] To understand whether and how the ligand requirements of OAS2 differ from those of other OAS proteins, we first analyzed the effects of RNA length dependence for the activation of OAS1, OAS2, and OAS3 (Figures 2A and 2B). In agreement with previous experiments, OAS1 is active when incubated with 22-bp-long dsRNA, and its activity increases gradually with longer RNAs.[37,38,49,61] In contrast, OAS2 is inactive with 22-bp-long dsRNA and shows minimal activity with 44 bp. Interestingly, the OAS2 enzyme exhibits proper activation only with long dsRNA of 82 bp. OAS3, on the other hand, is active in the presence of RNA with 44 bp length, and its activity only slightly increases even when incubated with longer RNAs. OAS1 p42 and OAS2 p69 demonstrated comparable activation behavior (Figure S3A). Accordingly, all subsequent experiments were conducted with OAS2 p71. Our results demonstrate that *in vitro* OAS2 requires longer RNAs than OAS3 for proper activation, supporting the hypothesis that the activation mechanism is more complex than the current model suggests. Next, we repeated this activity assay with OAS2 C652S and, interestingly, OAS2 C652S is even activated by dsRNA of 22 bp length in contrast to the wild-type protein, suggesting that binding of short RNA to the catalytically active OAS2 DII is sufficient for activation and that it is the dimerization that regulates its activation (Figure 2C). To investigate OAS protein activation in cells, we used a previously established biosensor for 2'-5'OA.[62] At first, it is evident that OAS3 produces more 2'-5'OA than OAS1 or OAS2, in line with previous reports[51,52,63–65] (Figures 2D, S3D, and S3E). Importantly, overexpression of OAS3 led to high 2′–5′OA synthesis in the absence of additional RNA stimulation. In contrast, OAS1 and OAS2 only became active after cells had been treated with poly I:C. This suggests that OAS3 may be activated by endogenous dsRNA sources in HEK293T or is not in an auto-repressed state. OAS1 p42 produced less 2′–5′OA, consistent with our *in vitro* experiments (Figures 2B, S3A, and S3D). These results indicate that the current activation model does not explain the differences observed for OAS2 RNA-mediated activation.

Please cite this article in press as: Merold et al., Structural basis for OAS2 regulation and its antiviral function, Molecular Cell (2025), https://doi.org/10.1016/j.molcel.2025.05.001

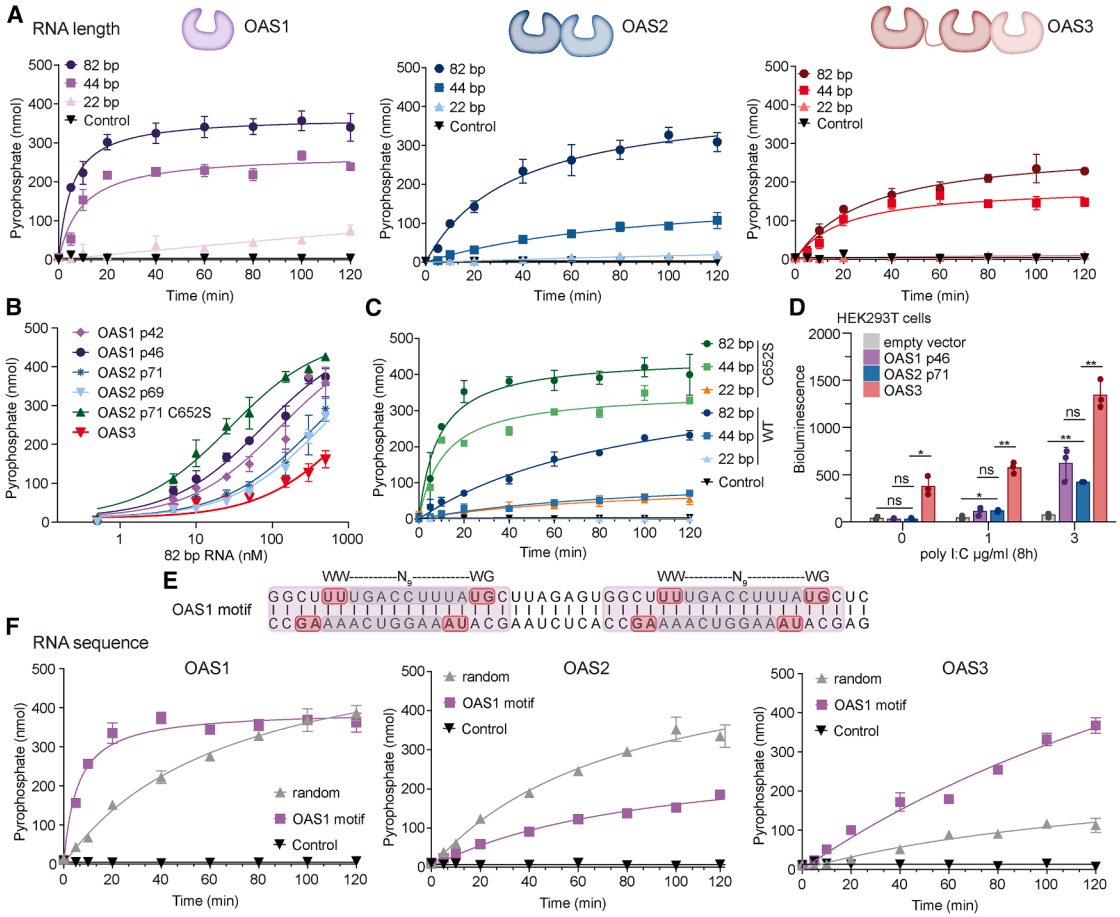

Figure 2. RNA ligand requirements for the activation of OAS2 differ from those of OAS1 and OAS3

(A) OAS protein activation by different RNA lengths. *In vitro* chromogenic activity assay of 200 nM OAS1 p46, OAS2 p71, and OAS3 p100, each with 22, 44, and 82 bp dsRNA (200 nM) (mean ± SD of $n = 3$).

(B) *In vitro* chromogenic activity assay showing dose response of OAS1 p42, OAS1 p46, OAS2 p69, OAS2 p71, OAS2 C652S, and OAS3 with 82 bp dsRNA (5, 10, 25, 50, 150, 300, and 500 nM) (mean ± SD of $n = 3$).

(C) *In vitro* assay as in (A) with 100 nM OAS2 wild type (blue) and OAS2 C652S (green, orange) with 23, 44, and 82 bp dsRNA (100 nM) (mean ± SD of $n = 3$).

(D) OAS protein activity in HEK293T cells measured with 2′-5′OA biosensor 8 h after poly I:C transfection (mean ± SD of $n = 3$). Paired *t* test: ns $p > 0.05$, * $p \leq 0.05$, ** $p \leq 0.01$.

(E) Sequence of preferred OAS1 motif. WWN9WG motif is colored in red. Repetitive sequence is colored in purple.

(F) Sequence preference of OAS proteins. *In vitro* assay as in (A) with 200 nM protein and 44 bp dsRNA (200 nM) containing OAS1 motif or random sequence (mean ± SD of $n = 3$).

See also Figure S3.

A conserved RNA motif WWN_9WG (where W can be either A or U and N can be any nucleotide) was demonstrated to strongly activate OAS1 (Figure 2E).[37,38,66–69] To determine whether OAS2 or OAS3 have the same sequence requirements as OAS1, we compared a 40-bp-long dsRNA with the duplicated conserved WWN_9WG motif (OAS1 motif) and one dsRNA containing a random sequence (Figure S3C). As expected, OAS1 activation was increased when incubated with the 40-bp RNA OAS1 motif (Figure 2F). OAS3 showed a similar behavior to OAS1, with the OAS1 motif activating the protein better than the random sequence. Interestingly, activation of OAS2 was stronger with random RNA sequence than with the OAS1 motif, confirming that OAS2 has different requirements for its ligand RNA sequence. However, for OAS2 protein activation, length takes precedence over sequence requirements, as 82 bp RNA no longer exhibits sequence-specific discrimination (Figure S3B).

OAS2 DI functions as a regulatory domain that measures RNA length using a non-canonical interface

Superposition of the OAS1-RNA complex structure onto DI and DII of the OAS2 dimer reveals that proposing an RNA-binding site spanning both OAS2 domains via the canonical binding interface is not feasible for two reasons (Figure S4A). First, the distance between the two interfaces cannot be extended by any 40-bp-long dsRNA. Second, the most notable feature of this interface on DI is the presence of a negatively charged surface, which is unfavorable for the binding of RNA (Figure S4B). To

Please cite this article in press as: Merold et al., Structural basis for OAS2 regulation and its antiviral function, Molecular Cell (2025), https://doi.org/10.1016/j.molcel.2025.05.001

CellPress
OPEN ACCESS

investigate how OAS2 DII and DI each contribute to the activation of OAS2 by RNA, we purified a construct of OAS2 DI. In agreement with previous reports, our experiments showed reduced binding to RNA for OAS2 DI, in contrast to significant binding of full-length OAS2 (Figure S4C). These results prompted us to further investigate the unknown contributions to RNA binding and the functional role of the DI in the activation mechanism of OAS2.

To characterize the conformational dynamics of OAS2 and to predict the RNA-binding site, we performed all-atom molecular dynamics (MD) simulations. The OAS2 dimer remains stable and close to the experimental cryo-EM structure (RMSD = 0.40 ± 0.06 nm) and shows low flexibility (Figure S4D). The monomeric OAS2 protein exhibits much higher flexibility (Figure S4D). Next, we used all-atom MD to predict the key residues involved in binding of dsRNA to OAS2. We performed conformational sampling at high and physiological temperatures and identified stable OAS2-RNA complexes. The results suggest that the RNA strongly bends along the dimer to span across DII and DI and introduces conformational changes at the interface connecting both monomers (Figure 3A). The identified key residues from this cryo-EM + MD approach relevant for the interactions of DI are depicted in Figures 3B and S4F. Although the residues identified on DII are in line with the OAS1-RNA-binding site, binding of dsRNA on DI occurs through a completely distinct interface, uncovering a non-canonical binding site specific to DI (Figures 3A, 3B, S4B, S4E, S4F, and S4J). Given that the RNA-binding site on DII is expected, we focused on the interactions between DI and RNA in the subsequent analysis. We performed further MD simulations focusing on the more active OAS2 monomer (Figures 3C and S4D). As a complementary approach, we used AF3 to predict the structure of the OAS2-RNA complex (Figures 3D and 3E).[59] The AF3 predictions for the monomeric OAS2 showed good agreement for the individual domains I (RMSD = 0.26 nm) and II (RMSD = 0.45 nm). Still, the overall structure deviated by 0.72 nm, indicating a conformational change in the orientation of the two domains. Therefore, we combined further MD simulations with the AF3 predictions (AF3 + MD approach) to identify additional key residues involved in RNA binding to OAS2 DI. To better illustrate the differences, we classified key residues of DI with higher contact frequencies to RNA into two distinct interfaces, labeled A and B (Figures 3B, 3F, 3G, S4F, and S4J). The AF3 + MD approach resulted in a less bent RNA compared with the results from the cryo-EM + MD method and showed more contacts with residues on DII (Figures 3C and 3D). Although the former does not indicate RNA contacts with residues in interface A, it does reveal interactions between the RNA and residues in the DI RNA-binding interface B, consistent with our cryo-EM + MD approach.

To validate the results from both approaches, we tested the effects of mutations at the predicted RNA-binding residues on OAS2 activation in cells. Nearly all tested mutations evidenced similar expression levels, except for R288A, suggesting that this mutation affects protein stability (Figures S4H and S4I). Additionally, nearly all mutated residues decreased OAS2 activation in cells, confirming that the predicted RNA-binding sites are necessary for OAS2 function (Figures 3H and 3I). Mutations of residues on DII (R529E R533E and K538E R544E) were chosen based on prior OAS–RNA structures and decreased OAS2 activity as expected (Figure S4G).[36–38,45] Notably, mutations on DI residues (R92, R165, D168, and K169) of interface B on the N-terminal lobe located more distantly from DII, demonstrated a significant effect on OAS2 activation (Figures 3H and 3I). Their location at the opposite end of the RNA relative to DII suggests that these residues distinguish between short and longer RNAs for activation (Figures 3F and 3J). Based on the integration of cryo-EM, MD simulations, and AF3 predictions, we propose that the cryo-EM + MD simulations approach illustrates the RNA-induced transition from the inactive cryo-EM dimer structure to the active monomeric state of the AF3 + MD predictions, which are most representative of the monomeric active conformation (Figure 3J). Our results define a mechanism of OAS2 activation in which RNA must bind to both domains DII and DI to induce the conformational changes necessary for activation. The catalytically inactive DI domain functions as a molecular ruler that measures and determines the minimum RNA length required for OAS2 activation.

OAS2 dimerization and localization to the Golgi membrane via myristoylation are required for activation

Blue-native polyacrylamide gel electrophoresis (PAGE) analysis showed that the wild-type OAS2 also forms a dimer in cells, whereas mutations in the zinc coordination site (C652S/H, H654S) resulted in monomeric OAS2 validating our cryo-EM structure (Figure 4A).[46] However, contrary to our biochemical *in vitro* findings, where OAS2 C652S was hyperactive in the presence of RNA, the monomeric OAS2 mutants displayed reduced activity compared with wild-type OAS2 in cells (Figures 4B, S5A, and S5B). These differences could not be explained by variations in expression levels or protein stability between OAS2 wild-type and mutant proteins (Figure S5C). We hypothesized that the mislocalization of the monomeric OAS2 mutants might explain the observed differences in activity. In BJ primary human foreskin fibroblasts (HFFs) and human lung adenocarcinoma A549 cells stimulated with interferon (IFN)-α, endogenous OAS2 localized to structures marked by the Golgi marker GM130 (Figures 4C, S5D, S5E, S5F, and S5G).[70] In A549 cells, endogenous OAS2 localized to *cis*-Golgi, medial-Golgi, and *trans*-Golgi networks, labeled by GM130, giantin, and TGN46, respectively,[71] but did not colocalize with the endoplasmic reticulum (ER) marker calnexin (Figures S5H and S5I). In addition, we demonstrate that OAS2 is oriented toward the cytosol and not localized in the Golgi lumen (Figure S5J).[72] Next, we generated A549 OAS2-knockout (KO) cells reconstituted with doxycycline-inducible OAS2 wild type, OAS2 C652S, and we also introduced the OAS2 G2A mutation, which disrupts a previously identified myristoylation site (Figure S5F).[54] We also confirmed that OAS2 is myristoylated in our experiments by mass spectrometry analysis (Figure S5K). The OAS2 G2A mutation disrupted OAS2 targeting to Golgi membranes, resulting in a diffuse cytosolic localization, and this applies to both OAS2 isoforms, p71 and p69 (Figures 4D, 4E, S6B, and S6C). Interestingly, OAS2 C652S also displayed a more diffuse cytosolic localization, with partial targeting to the Golgi, indicating an altered distribution compared with wild-type OAS2. These results reveal that OAS2 is a dimer localized to Golgi(-derived) membranes and

Please cite this article in press as: Merold et al., Structural basis for OAS2 regulation and its antiviral function, Molecular Cell (2025), https://doi.org/10.1016/j.molcel.2025.05.001

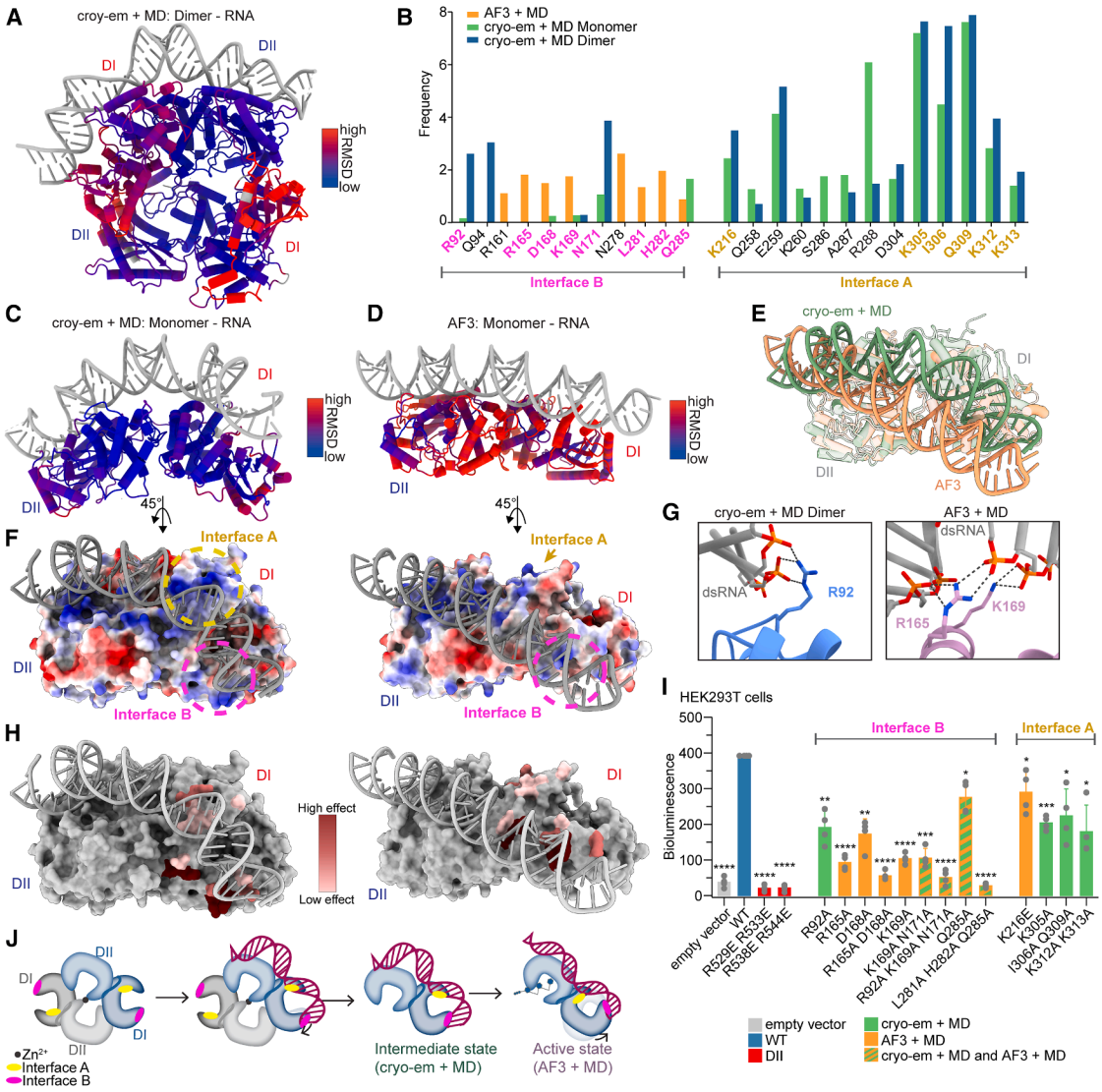

Figure 3. OAS2 DI functions as a regulatory domain that measures RNA length using a non-canonical interface

(A) MD simulation of OAS2 dimer in complex with dsRNA (gray), colored by RMSD values using the cryo-EM structure as a reference.

(B) Contact frequencies of DI with dsRNA, calculated based on cryo-EM + MD and AF3 + MD approaches. Residues tested in (I) are highlighted.

(C) MD simulation of OAS2 monomer in complex with dsRNA (gray). Structure is colored as in (A).

(D) AF3 prediction of OAS2 monomer in complex with dsRNA (gray). Structure is colored as in (A).

(E) Superposition of OAS2 with dsRNA from cryo-EM + MD and AF3 + MD approaches in green and orange, respectively.

(F) Electrostatic surface representation of monomeric OAS2 in complex with dsRNA from cryo-EM + MD (left) and AF3 prediction (right). Interfaces A and B are highlighted with yellow and pink dashed circles, respectively.

(G) Close ups of interface B from the cryo-EM + MD (left) and AF3 predicted structure (right).

(H) Surface view of structure depicted in (F), with color code indicating the effect of mutations from (I).

(I) OAS2 protein activity in HEK293T cells measured with 2′-5′OA biosensor (mean ± SD of $n = 3$). Paired t test: ns $p > 0.05$, * $p \leq 0.05$, ** $p \leq 0.01$, *** $p \leq 0.001$, **** $p \leq 0.0001$.

(J) Schematic overview of the RNA-binding mechanism of OAS2. The OAS2 dimer is auto-inhibited and, upon RNA binding, it monomerizes. The MD simulation illustrates an intermediate state, whereas the AF3 prediction more accurately represents the active state bound to RNA. RNA-binding interfaces A and B are colored in yellow and pink, respectively.

See also Figure S4.

that dimerization is required for the proper targeting of OAS2 to the Golgi.

To further define how the cellular localization of OAS2 impacts its activity, we investigated the activity of OAS2 wild type and the differently localizing OAS2 mutants C652S and G2A after stimulation with poly I:C. Unexpectedly, cytosolic OAS2 G2A showed no activity, indicating that Golgi localization is essential for OAS2 activation (Figures 4F, S6A, S6B, and

Please cite this article in press as: Merold et al., Structural basis for OAS2 regulation and its antiviral function, Molecular Cell (2025), https://doi.org/10.1016/j.molcel.2025.05.001

CellPress
OPEN ACCESS

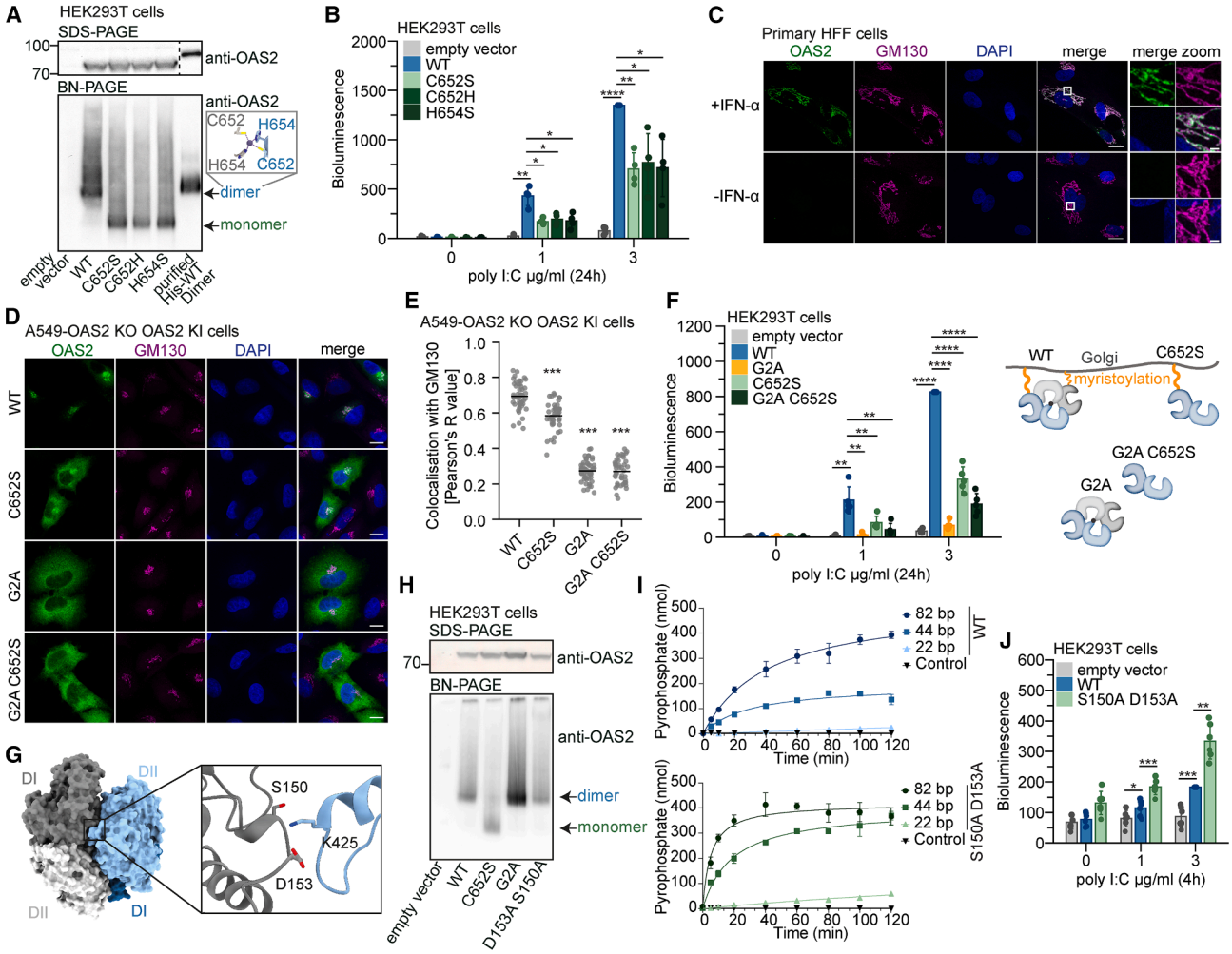

Figure 4. OAS2 dimerization and localization to the Golgi membrane via myristoylation are required for activation

(A) SDS-PAGE (top) and BN-PAGE (bottom) of OAS2 constructs transiently expressed in HEK293T cells and purified His-tagged OAS2 WT dimer. Zinc coordination is depicted on the right. SDS-PAGE was cut to remove a lane with marker.

(B) OAS2 activity in HEK293T cells measured with 2′–5′OA biosensor 24 h after poly I:C transfection, showing higher activity of dimeric OAS2 than the monomeric mutants.

(C) Immunofluorescence Airyscan microscopy of endogenous OAS2 localization in primary HFF cells stimulated with IFN-α and stained for OAS2 (green), Golgi marker GM130 (magenta), and DAPI (blue). Scale bars represent 20 µm and 2 µm for merge zoom.

(D) As in (C) for A549 *OAS2* KO cells reconstituted with doxycycline-inducible OAS2 constructs treated with doxycycline. Scale bars represent 10 µm.

(E) Quantification of colocalization of OAS2 constructs and Golgi marker GM130 from (D). Lines represent means from analyzed individual cells (dots). Student's *t* test with Welch's correction, $^{***}p \leq 0.001$.

(F) Analysis of OAS2 activity in cells as in (B) for OAS2 wild type and mutants with different localization showing that Golgi targeting is essential for the activity.

(G) Surface view of OAS2 dimer, with each monomer depicted in gray and blue. Close-up shows dimer interface interactions of S150 and D153.

(H) SDS-PAGE and BN-PAGE analysis as in (A).

(I) *In vitro* chromogenic activity assay with 200 nM OAS2 wild type and OAS2 S150A D153A with 23, 44, and 82 bp dsRNA (200 nM) (mean ± SD of $n = 3$).

(J) Analysis of OAS2 activity in cells as in (B) for OAS2 wild type and DI-DII interaction mutant S150A D153A.

In (B), (F), and (J) bars represent means ± SD of four (B), five (F), and six (J) independent replicates (dots). Paired *t* test: ns $p > 0.05$, $^{*}p \leq 0.05$, $^{**}p \leq 0.01$, $^{***}p \leq 0.001$, $^{****}p \leq 0.0001$.

See also Figures S5 and S6.

S6D), explaining why OAS2 C652S is less active in cells. To further demonstrate that the dimer-to-monomer transition induced by dsRNA is essential for OAS2 activation, we aimed to generate an OAS2 mutant that remains a dimer but has reduced affinity between the monomers. We targeted residues S150A D153A, which we predicted to have a lesser contribution to oligomerization than zinc-coordinating residues (Figure 4G). As expected, OAS2 S150A D153A was dimeric in cells and showed higher activity at earlier time points after poly I:C stimulation than OAS2 wild type in cells and *in vitro* (Figures 4H, 4I, 4J, S6E, and S6F). Our results demonstrate that, in addition to its RNA ligand, OAS2 requires both Golgi membrane targeting

Please cite this article in press as: Merold et al., Structural basis for OAS2 regulation and its antiviral function, Molecular Cell (2025), https://doi.org/10.1016/j.molcel.2025.05.001

via myristoylation and RNA-dependent dimer-to-monomer transition for activation.

These findings align with the recent discovery that OAS1 p46 is prenylated and targeted to membranes of the endomembrane system.[29,30,53,73] To discern the localization of OAS2 and OAS1 p46, we treated primary HFFs that express OAS2 and OAS1 p46 with IFN-α (Figure S6G). OAS1 partially colocalized with OAS2 but also exhibited a more diffuse localization that may correspond to its known localization in the ER (Figure S6H). To test how the precise membrane localization and orientation of the OAS domain relative to the membrane affects its activity, we designed a series of chimeric proteins where the N-terminal myristoylation motif and C-terminal prenylation motifs were swapped (Figures S6I, S6J, S6K, and S6L). The chimeric proteins did not produce any 2′–5′-OA, which may be due to reduced expression levels, e.g., OAS1 p46 chimera (Figures S6K and S6L). We performed the same experiment with OAS3, and targeting OAS3 to membranes not only prevented its activation in the absence of poly I:C stimulation but also reduced 2′–5′-OA production (Figures S6K and S6L). Together, our results define the cellular requirements for activation of OAS2: the localization and dimerization of OAS2 at the Golgi membrane are essential for its activation, and cytosolic RNA alone is insufficient to activate the protein in cells. These results challenge the previous dogma that OAS2 functions solely as a cytosolic RNA sensor.

OAS2 restricts viruses replicating at the endomembrane system

Several viruses are restricted by members of the OAS protein family, with OAS3 previously playing a dominant role in cytosolic viral RNA sensing.[52,63–65,74–76] To identify which viruses are sensed by OAS2 at the Golgi membrane and to further elucidate OAS2 activation in cells, we screened a panel of eleven GFP-reporter and non-reporter viruses for their replication in A549 *OAS2* KO cells that were reconstituted to express doxycycline-induced OAS2. Live cell imaging was conducted to analyze virus replication through GFP signal detection and to assess cell death using propidium iodide staining (Figures 5A, 5B, S7A, S7B, and S7C). Our panel of viruses included (1) flaviviruses YFV and ZIKV, which have positive-sense RNA genomes and replicate in ER-derived membranes; (2) negative-sense RNA viruses VSV and bunyaviruses BUNV, LACV, and RVFV, which replicate in the cytosol; (3) negative-sense RNA viruses IAV and THOV from the Orthomyxoviridae family, which replicate in the nucleus; (4) the positive-sense RNA virus EMCV, which replicates in ER/Golgi-derived organelles and double-membrane vesicles; and (5) dsDNA viruses HSV1 and VACV, which replicate in the nucleus and ER-enclosed sites in the cytosol, respectively. Of all the viruses tested, expression of OAS2 specifically reduced virus-induced cell death only during EMCV infection (Figures S7A and S7B), an effect that was not observed in cells expressing OAS2 C652S or OAS2 G2A (Figure 5B). Additionally, OAS2 expression significantly reduced intracellular EMCV RNA levels in an RNase L-dependent manner (Figures 5E and S8C). OAS2 localized to EMCV dsRNA but to a much lesser extent to YFV dsRNA during viral infection (Figures 5C, 5D, S8A, and S8B). Interestingly, OAS2 C652S showed less colocalization and OAS2 G2A was excluded from sites containing EMCV dsRNA (Figures 5C and 5D), clearly linking OAS2 localization with its antiviral effects.

EMCV is a cardiovirus that utilizes membranes from the endomembrane system to create viral replication organelles characterized by double-membrane vesicle (DMV) structures. Because EMCV was the only virus restricted by OAS2 in our screen, this raised the question of whether OAS2 may also restrict other viruses that utilize a similar replication strategy. Thus we selected enterovirus rhinovirus HRV16 and coronaviruses SARS-CoV-2, OC43, and NL63, which use Golgi or ER membranes for replication and form DMVs.[77] In HeLa H1 cells, HRV16 viral RNA levels and virus titers were significantly reduced upon overexpression of OAS2 p69 and, to a lesser extent, p71, as well as OAS1 p46 (Figures 5F, S8D, and S8E). OAS1 p46 localizes to the ER and Golgi and was used as a positive control here as it has previously been shown to restrict Rhinovirus replication.[30] Similarly, overexpression of OAS2 in HEK293T cells resulted only in a slight reduction in SARS-CoV-2 viral RNA levels but significantly reduced viral RNA levels for NL63 and OC43 (Figure 5G). There was also a reduction in OC43 virus titer in HEK293T cells and RNA levels upon OAS2 wild-type expression, but not OAS2 G2A and OAS2 C652S, in A549 *OAS2* KO cells in the absence, but not presence, of IFN-α pre-stimulation (Figures S8F and S8G). Taken together, our results show that OAS2 has evolved to restrict viruses that exploit the endomembrane system for replication to form viral replication organelles and DMVs.

OAS2 loss of function associated with immune dysregulation and ANCA vasculitis

To explore the relevance of our findings to human physiology, we analyzed patients with early onset immune dysregulation and identified a heterozygous *OAS2* variant in a child with autoinflammation and autoimmunity of unknown cause (extended case report in Data S1). The girl presented with rapidly progressive glomerulonephritis due to myeloperoxidase-anti-neutrophil cytoplasmic antibodies (MPO-ANCA)-associated vasculitis at the age of 4 years. (Figures 6A, 6B, and S9A.) Throughout the course of her disease, she was found to have elevated inflammatory markers (Figures 6A and S9A). Despite antibiotic and anti-inflammatory therapy, the hyperinflammation could not be controlled and the patient developed acute coronary syndrome with myocardial infarction with severe hemorrhagic complications. At the age of 6 years, the child suffered another hyperinflammatory episode with cytokine storm and succumbed to cardiocirculatory failure.

Whole-exome sequencing revealed a heterozygous *de novo* variant in *OAS2* (c.1572C>G, p.(Phe524Leu), GenBank: NM_002535.3) in the patient, affecting a highly conserved amino acid residue (Figures 6C, 6D, and S9B). No pathogenic variant or other variant of unknown significance in genes known to cause inborn errors of immunity or other syndromes associated with immune dysregulation were found. The F524L variant was not reported in the gnomAD database v4.1.0 and was predicted to be possibly damaging, with a PolyPhe-2 score of 0.953. Conservation of F524 extends beyond OAS2, as this residue is highly conserved in other proteins harboring the NTase fold (Figure 6E).[11] We mapped F524 to the catalytically active domain DII of OAS2 in our structure, where it is inserted into a

Please cite this article in press as: Merold et al., Structural basis for OAS2 regulation and its antiviral function, Molecular Cell (2025), https://doi.org/10.1016/j.molcel.2025.05.001

CellPress
OPEN ACCESS

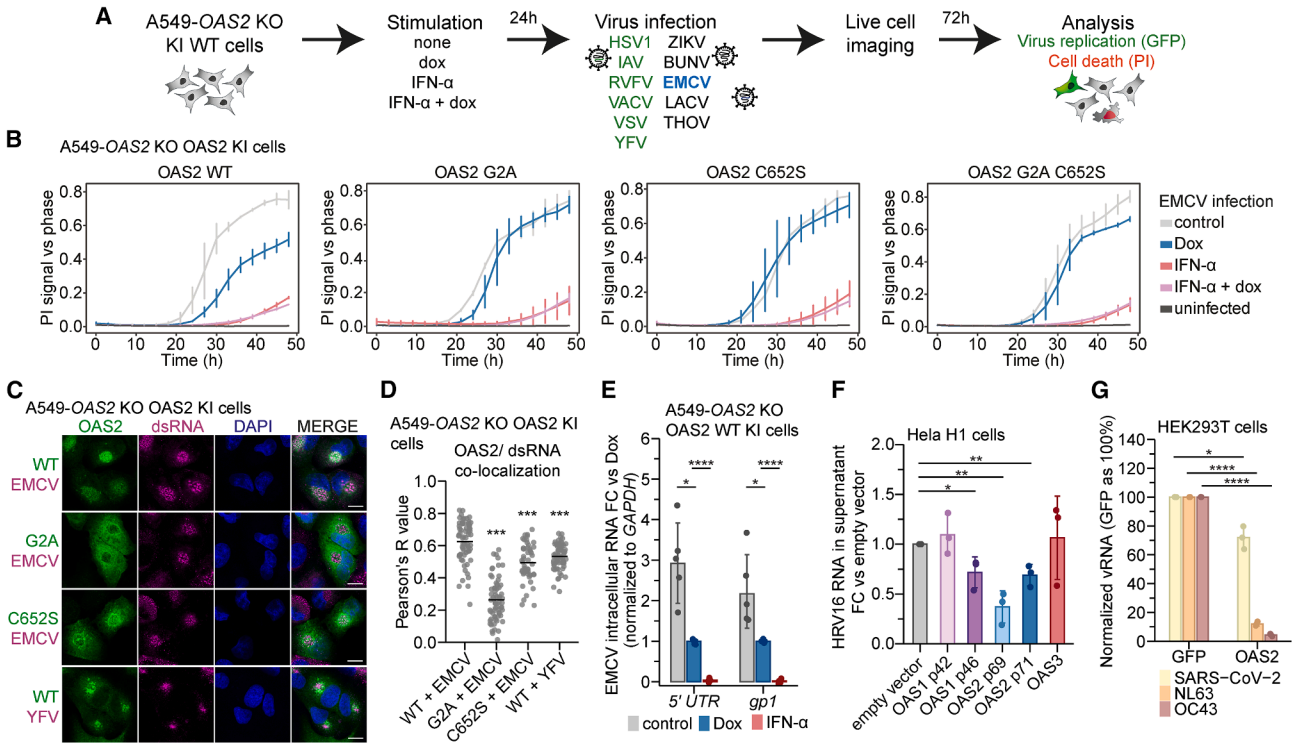

Figure 5. OAS2 restricts viruses replicating at the endomembrane system

(A) Experimental setup for virus screen (see STAR Methods). Cells were infected with a panel of GFP-reporter viruses (green) or non-reporter virus (black), followed by virus replication and cell death analysis.

(B) Cell death in EMCV-infected (MOI 0.3) A549 *OAS2* KO cells reconstituted with doxycycline-inducible OAS2 constructs (mean ± SD two technical replicates). Assays are representative of at least three independent experiments.

(C) Immunofluorescence Airyscan microscopy of OAS2 and viral dsRNA during EMCV and YFV infection in A549 *OAS2* KO cells reconstituted with doxycycline-inducible OAS2 constructs stained for OAS2 (green), dsRNA (magenta), and DAPI (blue). Scale bars represent 10 μm.

(D) Quantification of OAS2 and dsRNA colocalization from (C). Lines represent means from analyzed individual cells (dots). Student's *t* test with Welch's correction, $^{***}p \leq 0.001$.

(E) RT-qPCR analysis of intracellular EMCV RNA levels in A549 *OAS2* KO cells with KI for doxycycline-inducible OAS2 WT. Cells were treated with doxycycline or IFN-α followed by EMCV infection.

(F) RT-qPCR analysis of HRV16 viral RNA levels in Hela H1 cell supernatants. Cells were transiently transfected with different OAS constructs and infected with HRV16.

(G) RT-qPCR analysis of coronavirus RNA levels in culture supernatants in HEK293T cells overexpressing OAS2 WT.

In (E), (F), and (G) bars represent means ± SD of at least three independent experiments (dots). Paired *t* test in (E) and (G) and unpaired *t* test in (F). $^{*}p \leq 0.05$, $^{**}p \leq 0.001$, $^{***}p \leq 0.001$, $^{****}p \leq 0.0001$.

See also Figures S7 and S8.

hydrophobic pocket (Figure 6F). Other patient mutations R535Q, Q258L, and V290I on OAS2, previously identified in children with MIS-C, mapped to different sites: (i) R535 is located on a loop in DII close to the RNA-binding interface, while Q258L and V290I are in close proximity, located on DI (Figure S9C).[34] These mutations were described to have similar expression as wild-type OAS2 but with altered activity. Based on our structure and the effects of previous patient mutations, we predicted that mutation F524L would drastically disrupt protein structure and stability and thus cause a complete loss of function. Consistent with our predictions, patient fibroblasts showed significantly lower OAS2 protein expression and Golgi localization compared with wild-type fibroblasts (Figures 6G, 6H, 6I, and S9D). In agreement, activation of RNase L was significantly reduced in patient fibroblasts after treatment with poly I:C as well as in A549 *OAS2* KO cells reconstituted with OAS2 F524L (Figures 6J, S9E, and S9F). Overexpression of OAS2 F524L showed no activity, even 24 h after stimulation with poly I:C. In contrast, the previously reported R535Q patient mutation exhibited only reduced activity, indicating that F524L has a significantly stronger impact on OAS2 function (Figures 6K, S9G, and S9H). Our structural and biochemical findings reveal that dimerization of OAS2 is required for its function. Based on our findings, we hypothesize that the misfolded OAS2 F524L variant dimerizes with OAS2 wild type, and this leads to further destabilization and subsequent degradation of OAS2 wild type, resembling a dominant-negative effect. This could explain the very low OAS2 protein levels in patient cells treated with IFN-α—reduced by more than half (Figures 6G, 6H, and 6I)—and the pronounced phenotype despite the heterozygous mutation (Figures 6K, S9G, and

Please cite this article in press as: Merold et al., Structural basis for OAS2 regulation and its antiviral function, Molecular Cell (2025), https://doi.org/10.1016/j.molcel.2025.05.001

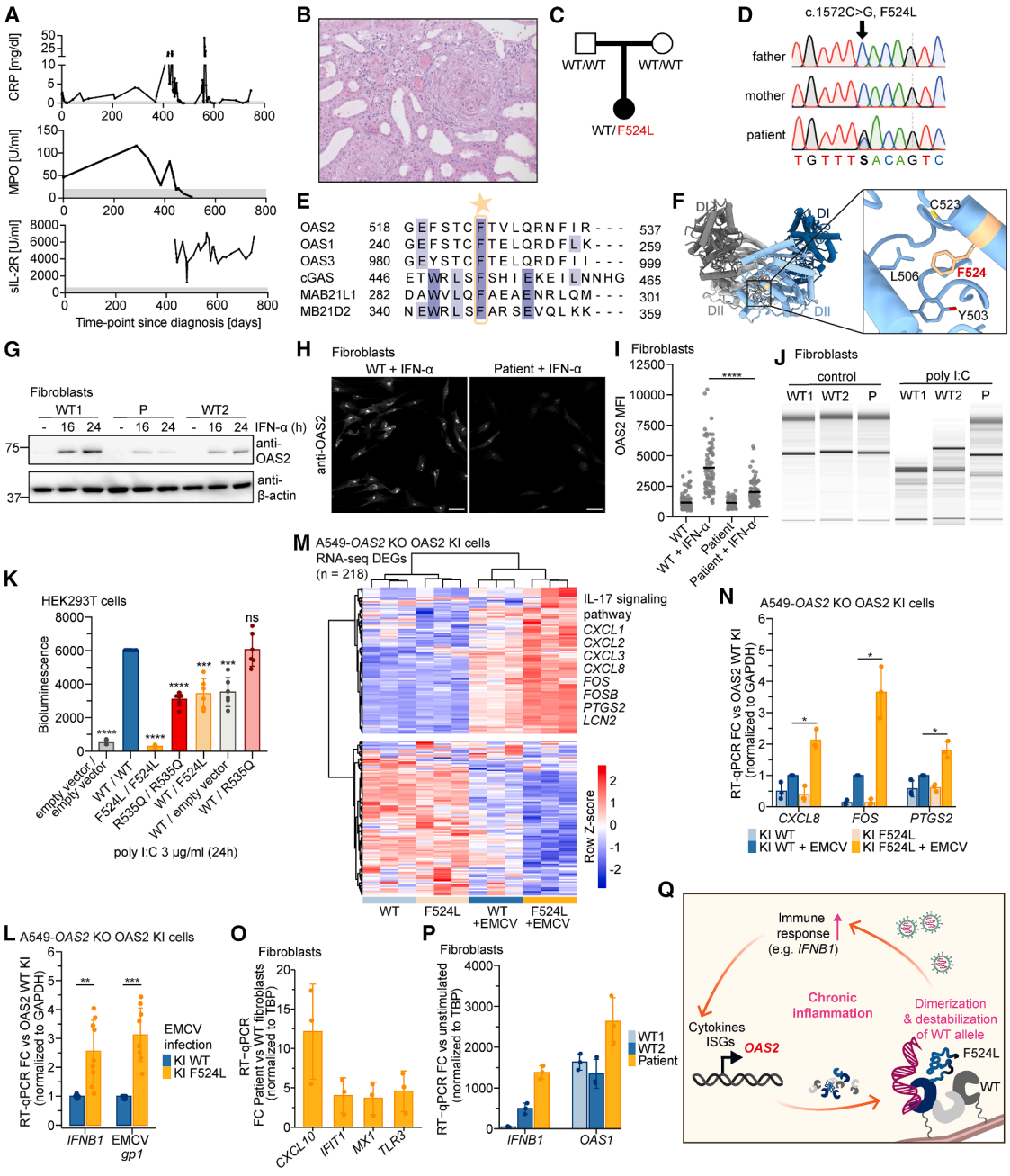

Figure 6. OAS2 loss of function is associated with immune dysregulation with ANCA vasculitis

(A) Patient's serum levels of inflammatory markers C-reactive protein (CRP; [<0.5 mg/dl] and soluble interleukin-2 receptor (sIL-2R; [158–613 U/ml]), and antibodies against myeloperoxidase (MPO; [<20 U/ml]). Gray bars indicate normal ranges.

(B) Renal biopsy with hematoxylin and eosin stain, 20x magnification.

(C) Pedigree of family with OAS2 F524L mutation.

(D) Electropherograms showing *de novo* heterozygous *OAS2* variant (c.1572C>G; p.Phe524Leu) by Sanger sequencing.

(E) Multiple sequence alignment of human OAS proteins and selected human NTases showing high conservation for F524 (yellow star).

(F) Structure of the OAS2 dimer with close-up view highlighting the amino acid F524.

(G) Expression levels of OAS2 in wild-type (WT) and patient fibroblasts treated with IFN-α ($n = 2$).

(H) OAS2 immunofluorescence staining in WT and patient fibroblasts treated with IFN-α. Scale bars represent 50 µm.

(I) Quantification of OAS2 mean fluorescence intensity from (H). Lines represent means from measurements of individual cells (dots). Student's *t* test with Welch's correction, **** $p \leq 0.0001$.

(J) RNA pico-chip analysis of total RNA isolated from wild-type (WT) and patient-derived fibroblast cell lines from control or poly I:C transfection.

(legend continued on next page)

Please cite this article in press as: Merold et al., Structural basis for OAS2 regulation and its antiviral function, Molecular Cell (2025), https://doi.org/10.1016/j.molcel.2025.05.001

CellPress
OPEN ACCESS

S9H). Next, we infected A549 OAS2 F524L cells with EMCV, a virus that we previously demonstrated to be restricted by OAS2 in Figure 5 (Figures 6L and S9I). RNA sequencing results revealed elevated responses to infection in A549 OAS2 F524L cells, with 191 differentially expressed genes (DEGs) when compared with 51 DEGs in A549 OAS2 WT cells (Figures 6M and S9J; Table S1). KEGG pathway analysis revealed that OAS2 loss of function results in upregulation of the inflammatory response to EMCV with an enrichment of genes from the IL-17 signaling pathway, such as *CXCL8*, *PTGS2*, and *FOS* (Figures 6M, 6N, and S9K). These findings are in line with inflammatory genes upregulated in THP-1 *OAS2* KO cells and myeloid cells from MIS-C patients with OAS–RNase L pathway deficiencies (Figure S9L).[34] Next, we analyzed inflammation markers in patient-derived fibroblasts: patient cells exhibited elevated basal levels of interferon-stimulated genes and inflammatory markers, such as *CXCL10*, *MX1*, *IFIT1*, and *TLR2* (Figure 6O). Upon stimulation with poly I:C, patient fibroblasts showed further elevated levels, leading to an amplified interferon-stimulated gene (ISG) response compared with wild-type cells (Figure 6P). In addition, elevated upregulation of ISG expression potentially leads to increased expression of OAS2 wild type and the OAS2 F524L variant in patient cells. This further supports our proposed mechanism in which the destabilization of both OAS2 F524L and OAS2 wild-type proteins leads to lower protein levels in patient cells despite the higher mRNA levels upon stimulation. Additionally, patient cells showed slower proliferation and reduced translational activity compared with wild-type controls (Figures S9M, S9N, and S9O). Together, our results describe a plausible mechanism explaining how the OAS2 F524L mutation can contribute to the patient's inflammatory phenotype (Figure 6Q), where the loss of OAS2 function, which, upon stimulation, exacerbates the immune response, contributes to severe autoinflammatory and autoimmune disease.

DISCUSSION

Historically, OAS protein activation has been primarily characterized by its convergence on RNase L activation, with little understanding of the distinct antiviral roles of various OAS genes and even less clarity regarding the different isoforms of OAS genes. In this context, it has been widely described that OAS proteins have evolved to recognize different RNA ligands of varying lengths.[60,78–82] However, the mechanism for length discrimination by members of the OAS protein family with multiple OAS domains remained unclear. The loss of catalytic activity in certain OAS domains has further hindered our understanding of the OAS protein family's function. Previous data suggested that both domains of OAS2 are required for activation, as the isolated catalytically active domain DII of OAS2 was unexpectedly found to be inactive in the presence of RNA.[44,46–48] Our data on the dimeric structure of OAS2 explain the underlying mechanism: domain DII is held in an inactive conformation via zinc coordination, while DI provides the necessary trigger to release DII from the inactive conformation after RNA binding. Auto-inhibition of OAS2 by dimerization represents a mechanism for RNA length discrimination in the OAS protein family and shows how OAS2 is prevented from being activated by shorter RNAs, thereby avoiding autoreactivity. This regulatory mechanism, unique to OAS2, also explains its different ligand requirements compared with OAS1 and OAS3.

The recent discovery that prenylation of the OAS1 p46 targets OAS1 to membranes of the endomembrane system for virus detection has sparked a new perspective on investigating the non-redundant roles of OAS proteins.[29,30] Our results showing that proper targeting of OAS2 to the Golgi by myristoylation is required for OAS2 activation further support the notion that OAS proteins have evolved not only to recognize different RNA ligands but also, more importantly, to restrict viral replication at different subcellular localizations. Its localization at the Golgi membrane allows OAS2 to specifically detect viruses that utilize membranes to form replication organelles with DMV structures and that would otherwise effectively protect their RNA from being recognized by the immune system. This feature distinguishes the antiviral repertoire of OAS2 from that of other RNA sensors, such as OAS3, which senses viruses that replicate in the cytosol.[52] Positioning of OAS proteins at viral replication organelles (i.e., sites that are rich in viral RNA, increasing the local OAS2 concentrations) would also explain why OAS proteins can sense slight changes in dsRNA in cells despite the previously observed relatively low affinities of OAS1 and OAS2 for RNA.[47,68,80,83] In addition, differences in virus restriction among members of the OAS family may also be attributed to evasion mechanisms that viruses have evolved.[84]

We identified a child with a heterozygous *de novo* mutation in OAS2, F524L, who developed severe autoinflammation and autoimmunity. Unlike the hypomorphic OAS2 mutations associated with MIS-C, F524L leads to OAS2 loss of function by destabilizing its structure. Our results suggest a possible mechanism: reduced OAS2 expression could be attributed to the unstable OAS2 F524L variant dimerizing with the wild-type OAS2 protein, leading to dimer destabilization. Consequently, the dimer would

(K) Analysis of OAS2 protein activity in HEK293T cells with 2′–5′OA biosensor 24 h after poly I:C transfection for OAS2 wild type and patient mutations F524L and R535Q (mean ± SD of $n = 6$).
(L) RT-qPCR analysis of *IFNB1* and intracellular EMCV RNA levels for *gp1* in A549-*OAS2* KO cells with KI for doxycycline-inducible OAS2 WT and OAS2 F524L. Cells were treated with doxycycline followed by EMCV infection (mean ± SD of $n = 9$).
(M) RNA-seq heatmap of normalized counts of DEGs from A549-*OAS2* KO cells reconstituted with doxycycline-inducible OAS2 WT and OAS2 F524L, with or without EMCV infection. Clustering identified two clusters, with IL-17 signaling pathway genes enriched in the top cluster.
(N) RT-qPCR analysis as in (L) (mean ± SD of $n = 3$).
(O) RT-qPCR analysis of patient and WT fibroblasts (3 donors) in basal unstimulated conditions. (Mean ± SD.)
(P) RT-qPCR analysis of patient and WT fibroblasts stimulated with poly I:C (mean ± SD of $n = 3$).
(Q) Summary schematic of the model of heterozygous OAS2 F524L mutation pathogenesis in inflammation.
In (K), (L), and (N) statistical significance was calculated using paired *t* test. ns $p > 0.05$, * $p \leq 0.05$, ** $p \leq 0.001$, ***$p \leq 0.001$, **** $p \leq 0.0001$.
See also Figure S9, Data S1, and Table S1.

Please cite this article in press as: Merold et al., Structural basis for OAS2 regulation and its antiviral function, Molecular Cell (2025), https://doi.org/10.1016/j.molcel.2025.05.001

Table 1. Cryo-EM data collection, 3D reconstruction, and model refinement statistics

	OAS2 apo (EMD:51786) (PDB 9H1Z)
Data collection and processing	
Magnification	130,000
Voltage (kV)	300
Electron exposure (e–/Å^2)	50
Defocus range (μm)	−1.4 to −2.9
Pixel size (Å)	1.059
Symmetry imposed	C2
Initial particle images (no.)	2,914,103
Final particle images (no.)	532,195
Map resolution (Å)	3.31
0.143 FSC threshold	–
Map resolution range (Å)	2.8–5
Refinement	
Initial model used (PDB code)	AF2 AF-P29728-F1
Model resolution (Å)	3.48
0.5 FSC threshold	–
Model resolution range (Å)	80–3.2
Map sharpening *B* factor (Å^2)	−84.47
Model composition	
Non-hydrogen atoms	10,747
Protein residues	1,323
Ligands	1
B factors (Å^2)	
Protein	77.42
Ligand	43.62
R.m.s. deviations	
Bond lengths (Å)	0.003
Bond angles (°)	0.562
Validation	
MolProbity score	1.59
Clashscore	6.36
Poor rotamers (%)	0
Ramachandran plot	
Favored (%)	95
Allowed (%)	5
Disallowed (%)	0

no longer be activated by RNA, resulting in a loss of function. In line with observations in MIS-C patients, loss of function of OAS2 led to an elevated immune response in A549 cells expressing OAS2 F524L and patient cells, including increased IFNβ and ISG levels. This response drives increased expression of OAS genes, including OAS2 and the unstable OAS2 F524L variant. The heightened expression of OAS2 F524L further amplifies the inflammatory loop, reinforcing the ongoing interferon response, creating a vicious cycle that can lead to autoinflammation and autoimmunity. In addition, the elevated basal levels of inflammatory markers detected in patient fibroblasts suggest a state of chronic interferon activation in the patient. Even if some residual activity of OAS2 wild type is present in patient cells, it is most likely not sufficient to restrict the virus. This is supported by experiments using OAS2 C652S, which, despite showing partial activity, failed to restrict replication of EMCV and OC43 viruses compared with OAS2 wild type. The associated phenotype of autoinflammation and autoimmunity supports the idea that OAS proteins have evolved to restrict different viruses and that these have non-redundant roles in antiviral immunity. It is tempting to speculate that the patient was infected with a common cold virus, such as coronaviruses or rhinoviruses, which are restricted by OAS2 and not usually tested for during hospitalization. Persistent infection due to defective restriction of the virus may have been the trigger for the autoinflammatory and autoimmune phenotype, as seen in the exacerbated inflammatory response in our transcriptomic analysis of infected A549 OAS2 F524L cells. Our results reveal mechanisms of auto-inhibition and activation of a multi-domain OAS protein, illustrate how subcellular localization in cells is required for OAS2 to exert its antiviral function, and highlight the clinical relevance of OAS2.

Limitations of the study

We propose a possible mechanism explaining how a loss-of-function mutation in OAS2 could contribute to the severe autoimmune disease observed in the patient. A limitation of our study is the absence of a rescue experiment in patient cells, which would be necessary to establish causality and rule out the possibility that other genetic variants may also contribute to the disease. Furthermore, our experimental setup does not allow us to determine whether the OAS2 F524L variant exerts a dominant-negative effect. Further work is required to clarify whether OAS2 F524L exerts a dominant-negative effect and how this may lead to the severe autoimmune disease. Future research will also be critical to elucidate the differences in virus restriction mechanisms employed by OAS1 and OAS2 within the endomembrane system, potentially explaining the non-redundant roles of these OAS proteins. Our data reveal that OAS1 and OAS2 are regulated by distinct mechanisms and suggest that they may be activated by different ligands. However, further investigations are needed to fully characterize the nature of the preferred physiological dsRNA ligands for OAS proteins.

RESOURCE AVAILABILITY

Lead contact

Further information and request for data and resources should be directed to, and will be fulfilled by, the lead contact, Carina C. de Oliveira Mann (carina.mann@tum.de).

Materials availability

All unique/stable reagents generated in this study are available from the lead contact upon reasonable request.

Data and code availability

- The coordinates of OAS2 apo structure have been deposited in the Protein Data Bank (PDB) under the accession number PDB: 9H1Z, and the cryo-EM reconstruction is available in the Electron Microscopy Bank (EMDB) under the accession number EMD-51786. The MD simulation data are deposited in zenodo.org (https://doi.org/10.5281/zenodo.14753364). RNA sequencing (RNA-seq) data have been deposited in

Please cite this article in press as: Merold et al., Structural basis for OAS2 regulation and its antiviral function, Molecular Cell (2025), https://doi.org/10.1016/j.molcel.2025.05.001

CellPress
OPEN ACCESS

ArrayExpress with accession code E-MTAB-14791. Unprocessed western blot and microscopy images from this study were deposited on Mendeley Data: https://doi.org/10.17632/tvgpf9t2jm.1. These data are publicly available as of the date of publication.

- This paper does not report original code.
- Any additional information required to reanalyze the data reported in this paper is available from the lead contact upon request.

ACKNOWLEDGMENTS

We thank members of the NTase laboratory for helpful comments and discussion. 2′-5′OA biosensors were kindly provided by A. Korennykh, Princeton University. We thank K. Krey for help with virus infections and IncuCyte experiments and K. Austen for assistance with Airyscan microscopy. We thank J.-R. Fischer and B. Ott for technical assistance; L. Kuhn, P. Ascanio, and S. D'Souza for cloning; and G. Witte for advice on mass photometry. We are thankful to K. Amann, Institute of Pathology, FAU Erlangen-Nürnberg, for renal histology. We acknowledge the scientific support and HPC resources provided by the Erlangen National High-Performance Computing Center (NHR@FAU) of the Friedrich-Alexander-Universität Erlangen-Nürnberg under the NHR project b119ee.

The work was funded by the German Research Foundation Emmy Noether Program 458004906 (C.C.O.M.); CRC237 369799452/A25/A11,B11/A07/A28 (C.C.O.M., M.L.-K., A.P., and L.K.); CRC179 272983813/TP24N (A.P.); CRC353 471011418/B04 (A.P.); CRC369 501752319/C06 (M.L.-K.); CRC1279/A08, SP 1600/7-1, and SP 1600/9-1 (K.M.J.S.); Sachbeihilfe grant KM 5/3-1 (D.K.) and 52953824 (N.S. and A.S.); European Research Council ERC-StG-2023 101117085 (C.C.O.M.); German Federal Ministry of Education and Research (BMBF) in the framework of the Cluster4Future program (CNATM, 03ZU1201BA, C.C.O.M.); BMBF IMMUNOMOD-01KI2014 (K.M.J.S.), 01GM2206C (GAIN, M.L.-K.), and 01GL2405H (DZKJ, M.L.-K.). K.M.J.S is supported by the Baden-Wuerttemberg Stiftung (AutophagyBoost). I.B. is supported by a DFG Walter Benjamin Fellowship. R.S. and D.K. were supported by a Baustein grant of the Medical Faculty, Ulm University. This work was funded in part by the German Research Foundation (INST 95/1650-1 FUGG).

AUTHOR CONTRIBUTIONS

The project was conceived, and experiments designed, by V.M., I.B., and C.C.O.M. V.M. prepared and screened cryo-EM samples and performed biochemical analysis with assistance from S.H. and C.C.O.M. K.L. collected cryo-EM data. V.M. performed structure determination and model building with assistance from K.L. and C.C.O.M. MD simulations were performed by A.S. and N.S. I.B. performed cell-based assays and fluorescence microscopy. M.H. quantified fluorescence microscopy images. I.B., D.K., R.S., and A.H. performed virus infections under supervision of C.C.O.M., A.P., and K.M.J.S. I.B. prepared samples for mass spectrometry and J.M. collected and analyzed data. S.K., R.L., K.H., and I.B. performed patient-related experiments under supervision of M.L.-K. and C.C.O.M. M.L.-K. analyzed genomic patient data and supervised patient-related experiments and interpreted data. K.B. and M.W. contributed patient data. J.T. and L.M.K. provided *in vitro* transcription (IVT) RNA. The manuscript was written by V.M., I.B., and C.C.O.M., and all authors contributed to editing the manuscript and support the conclusions.

DECLARATION OF INTERESTS

L.M.K. is an employee at BioNTech without relation to this work.

STAR★METHODS

Detailed methods are provided in the online version of this paper and include the following:

- KEY RESOURCES TABLE
- EXPERIMENTAL MODEL AND STUDY PARTICIPANT DETAILS
  - Escherichia coli strains
  - Virus strains
  - Insect cell lines
  - Mammalian cell lines and primary cells
- METHOD DETAILS
  - Protein expression and purification
  - Cryo-electron microscopy grid preparation
  - Cryo-electron microscopy data acquisition
  - Cryo-electron microscopy data processing
  - Model building and Figure preparation
  - In-vitro OAS activity assay
  - EMSA (electrophoretic mobility shift assay)
  - In-vitro Transcription
  - Mass photometry
  - MD simulations
  - Simulation setup
  - OAS2 monomer and dimer simulations
  - dsRNA binding site prediction simulations
  - Number of close contacts
  - Contact frequencies
  - RMSD
  - Generation of cell lines
  - 2′-5′ oligoadenylate (OA) biosensor analysis
  - Western Blot analysis
  - BN-PAGE analysis
  - Immunofluorescence staining and imaging
  - Live cell imaging of viral replication
  - Viral RNA detection
  - RT-qPCR analysis
  - RNA-seq and data processing
  - Virus titer measurements
  - Protein synthesis assay
  - Proliferation assay
  - RNA degradation assay
  - Immunoprecipitation and mass spectrometry
  - Genetic investigations
  - Sanger sequencing
- QUANTIFICATION AND STATISTICAL ANALYSIS

SUPPLEMENTAL INFORMATION

Supplemental information can be found online at https://doi.org/10.1016/j.molcel.2025.05.001.

Received: October 11, 2024
Revised: February 1, 2025
Accepted: May 1, 2025
Published: May 23, 2025

REFERENCES

1. Roberts, W.K., Clemens, M.J., and Kerr, I.M. (1976). Interferon-induced inhibition of protein synthesis in L-cell extracts: an ATP-dependent step in the activation of an inhibitor by double-stranded RNA. Proc. Natl. Acad. Sci. USA. *73*, 3136–3140. https://doi.org/10.1073/pnas.73.9.3136.
2. Williams, B.R.G., Kerr, I.M., Gilbert, C.S., White, C.N., and Ball, L.A. (1978). Synthesis and Breakdown of pppA2'p5'A2'p5'A and Transient Inhibition of Protein Synthesis in Extracts from Interferon-Treated and Control Cells. Eur. J. Biochem. *92*, 455–462. https://doi.org/10.1111/j.1432-1033.1978.tb12767.x.
3. Minks, M.A., Benvin, S., and Baglioni, C. (1980). Mechanism of pppA(2'p5'A)n2'p5'AOH synthesis in extracts of interferon-treated HeLa cells. J. Biol. Chem. *255*, 5031–5035. https://doi.org/10.1016/S0021-9258(19)70744-3.

4. Minks, M.A., West, D.K., Benvin, S., and Baglioni, C. (1979). Structural requirements of double-stranded RNA for the activation of 2′,5′-oligo(A) polymerase and protein kinase of interferon-treated HeLa cells. J. Biol. Chem. *254*, 10180–10183. https://doi.org/10.1016/S0021-9258(19)86690-5.

5. Hovanessian, A.G., Svab, J., Marié, I., Robert, N., Chamaret, S., and Laurent, A.G. (1988). Characterization of 69- and 100-kDa forms of 2–5A-synthetase from interferon-treated human cells. J. Biol. Chem. *263*, 4945–4949. https://doi.org/10.1016/S0021-9258(18)68878-7.

6. Lebleu, B., Sen, G.C., Shaila, S., Cabrer, B., and Lengyel, P. (1976). Interferon, double-stranded RNA, and protein phosphorylation. Proc. Natl. Acad. Sci. USA. *73*, 3107–3111. https://doi.org/10.1073/pnas.73.9.3107.

7. Hovanessian, A.G., Laurent, A.G., Chebath, J., Galabru, J., Robert, N., and Svab, J. (1987). Identification of 69-kd and 100-kd forms of 2–5A synthetase in interferon-treated human cells by specific monoclonal antibodies. EMBO J. *6*, 1273–1280. https://doi.org/10.1002/j.1460-2075.1987.tb02364.x.

8. Hovanessian, A.G., and Kerr, I.M. (1978). Synthesis of an oligonucleotide inhibitor of protein synthesis in rabbit reticulocyte lysates analogous to that formed in extracts from interferon-treated cells. Eur. J. Biochem. *84*, 149–159. https://doi.org/10.1111/j.1432-1033.1978.tb12151.x.

9. Hovanessian, A.G., and Kerr, I.M. (1979). The (2'-5') oligoadenylate (pppA2'-5'A2'-5'A) synthetase and protein kinase(s) from interferon-treated cells. Eur. J. Biochem. *93*, 515–526. https://doi.org/10.1111/j.1432-1033.1979.tb12850.x.

10. Kerr, I.M., and Brown, R.E. (1978). pppA2'p5'A2'p5'A: an inhibitor of protein synthesis synthesized with an enzyme fraction from interferon-treated cells. Proc. Natl. Acad. Sci. USA. *75*, 256–260. https://doi.org/10.1073/pnas.75.1.256.

11. Kuchta, K., Knizewski, L., Wyrwicz, L.S., Rychlewski, L., and Ginalski, K. (2009). Comprehensive classification of nucleotidyltransferase fold proteins: identification of novel families and their representatives in human. Nucleic Acids Res. *37*, 7701–7714. https://doi.org/10.1093/nar/gkp854.

12. Hornung, V., Hartmann, R., Ablasser, A., and Hopfner, K.P. (2014). OAS proteins and cGAS: unifying concepts in sensing and responding to cytosolic nucleic acids. Nat. Rev. Immunol. *14*, 521–528. https://doi.org/10.1038/nri3719.

13. Hovanessian, A.G., Brown, R.E., and Kerr, I.M. (1977). Synthesis of low molecular weight inhibitor of protein synthesis with enzyme from interferon-treated cells. Nature *268*, 537–540. https://doi.org/10.1038/268537a0.

14. Hovanessian, A.G., and Justesen, J. (2007). The human 2'-5′oligoadenylate synthetase family: unique interferon-inducible enzymes catalyzing 2'-5′ instead of 3′-5′ phosphodiester bond formation. Biochimie *89*, 779–788. https://doi.org/10.1016/j.biochi.2007.02.003.

15. Sarkar, S.N., Bandyopadhyay, S., Ghosh, A., and Sen, G.C. (1999). Enzymatic characteristics of recombinant medium isozyme of 2'-5′ oligoadenylate synthetase. J. Biol. Chem. *274*, 1848–1855. https://doi.org/10.1074/jbc.274.3.1848.

16. Ghosh, A., Sarkar, S.N., and Sen, G.C. (2000). Cell Growth Regulatory and Antiviral Effects of the P69 Isozyme of 2–5 (A) Synthetase. Virology *266*, 319–328. https://doi.org/10.1006/viro.1999.0085.

17. Bandyopadhyay, S., Ghosh, A., Sarkar, S.N., and Sen, G.C. (1998). Production and Purification of Recombinant 2'-5. Biochemistry *37*, 3824–3830. https://doi.org/10.1021/bi972848e.

18. Dong, B., Xu, L., Zhou, A., Hassel, B.A., Lee, X., Torrence, P.F., and Silverman, R.H. (1994). Intrinsic molecular activities of the interferon-induced 2–5A-dependent RNase. J. Biol. Chem. *269*, 14153–14158. https://doi.org/10.1016/S0021-9258(17)36767-4.

19. Banerjee, S., Chakrabarti, A., Jha Babal, K., Weiss Susan, R., and Silverman Robert, H. (2014). Cell-Type-Specific Effects of RNase L on Viral Induction of Beta Interferon. mBio *5*, qq. https://doi.org/10.1128/mbio.00856-00814.

20. Han, Y., Whitney, G., Donovan, J., and Korennykh, A. (2012). Innate immune messenger 2–5A tethers human RNase L into active high-order complexes. Cell Rep. *2*, 902–913. https://doi.org/10.1016/j.celrep.2012.09.004.

21. Huang, H., Zeqiraj, E., Dong, B., Jha, B.K., Duffy, N.M., Orlicky, S., Thevakumaran, N., Talukdar, M., Pillon, M.C., Ceccarelli, D.F., et al. (2014). Dimeric structure of pseudokinase RNase L bound to 2–5A reveals a basis for interferon-induced antiviral activity. Mol. Cell *53*, 221–234. https://doi.org/10.1016/j.molcel.2013.12.025.

22. Han, Y., Donovan, J., Rath, S., Whitney, G., Chitrakar, A., and Korennykh, A. (2014). Structure of human RNase L reveals the basis for regulated RNA decay in the IFN response. Science *343*, 1244–1248. https://doi.org/10.1126/science.1249845.

23. Donovan, J., Rath, S., Kolet-Mandrikov, D., and Korennykh, A. (2017). Rapid RNase L-driven arrest of protein synthesis in the dsRNA response without degradation of translation machinery. RNA *23*, 1660–1671. https://doi.org/10.1261/rna.062000.117.

24. Silverman, R.H. (2007). Viral Encounters with 2′,5′-Oligoadenylate Synthetase and RNase L during the Interferon Antiviral Response. J. Virol. *81*, 12720–12729. https://doi.org/10.1128/JVI.01471-07.

25. Hovanessian, A.G., Wood, J., Meurs, E., and Montagnier, L. (1979). Increased nuclease activity in cells treated with pppA2'p5'A2'p5' A. Proc. Natl. Acad. Sci. USA. *76*, 3261–3265. https://doi.org/10.1073/pnas.76.7.3261.

26. Magusali, N., Graham, A.C., Piers, T.M., Panichnantakul, P., Yaman, U., Shoai, M., Reynolds, R.H., Botia, J.A., Brookes, K.J., Guetta-Baranes, T., et al. (2021). A genetic link between risk for Alzheimer's disease and severe COVID-19 outcomes via the OAS1 gene. Brain *144*, 3727–3741. https://doi.org/10.1093/brain/awab337.

27. Magg, T., Okano, T., Koenig, L.M., Boehmer, D.F.R., Schwartz, S.L., Inoue, K., Heimall, J., Licciardi, F., Ley-Zaporozhan, J., Ferdman, R.M., et al. (2021). Heterozygous *OAS1* gain-of-function variants cause an autoinflammatory immunodeficiency. Sci. Immunol. *6*, eabf9564. https://doi.org/10.1126/sciimmunol.abf9564.

28. Padhi, S., Sarangi, S., Nayak, N., Pati, A., and Panda, A.K. (2022). OAS1 rs1131454 genetic variant is associated with Alzheimer's disease: an epidemiological analysis. Brain *145*, e61–e63. https://doi.org/10.1093/brain/awac132.

29. Wickenhagen, A., Sugrue, E., Lytras, S., Kuchi, S., Noerenberg, M., Turnbull, M.L., Loney, C., Herder, V., Allan, J., Jarmson, I., et al. (2021). A prenylated dsRNA sensor protects against severe COVID-19. Science *374*, eabj3624. https://doi.org/10.1126/science.abj3624.

30. Soveg, F.W., Schwerk, J., Gokhale, N.S., Cerosaletti, K., Smith, J.R., Pairo-Castineira, E., Kell, A.M., Forero, A., Zaver, S.A., Esser-Nobis, K., et al. (2021). Endomembrane targeting of human OAS1 p46 augments antiviral activity. eLife *10*, e71047. https://doi.org/10.7554/eLife.71047.

31. Zhou, S., Butler-Laporte, G., Nakanishi, T., Morrison, D.R., Afilalo, J., Afilalo, M., Laurent, L., Pietzner, M., Kerrison, N., Zhao, K., et al. (2021). A Neanderthal OAS1 isoform protects individuals of European ancestry against COVID-19 susceptibility and severity. Nat. Med. *27*, 659–667. https://doi.org/10.1038/s41591-021-01281-1.

32. Banday, A.R., Stanifer, M.L., Florez-Vargas, O., Onabajo, O.O., Papenberg, B.W., Zahoor, M.A., Mirabello, L., Ring, T.J., Lee, C.H., Albert, P.S., et al. (2022). Genetic regulation of OAS1 nonsense-mediated decay underlies association with COVID-19 hospitalization in patients of European and African ancestries. Nat. Genet. *54*, 1103–1116. https://doi.org/10.1038/s41588-022-01113-z.

33. Huffman, J.E., Butler-Laporte, G., Khan, A., Pairo-Castineira, E., Drivas, T.G., Peloso, G.M., Nakanishi, T., Ganna, A., Verma, A., et al.; COVID-19 Host Genetics Initiative (2022). Multi-ancestry fine mapping implicates OAS1 splicing in risk of severe COVID-19. Nat. Genet. *54*, 125–127. https://doi.org/10.1038/s41588-021-00996-8.

Please cite this article in press as: Merold et al., Structural basis for OAS2 regulation and its antiviral function, Molecular Cell (2025), https://doi.org/10.1016/j.molcel.2025.05.001

34. Lee, D., Le Pen, J., Yatim, A., Dong, B., Aquino, Y., Ogishi, M., Pescarmona, R., Talouarn, E., Rinchai, D., Zhang, P., et al. (2022). Inborn errors of OAS–RNase L in SARS-CoV-2-related multisystem inflammatory syndrome in children. Science *377*, eabo3627. https://doi.org/10.1126/science.abo3627.

35. Chebath, J., Benech, P., Hovanessian, A., Galabru, J., and Revel, M. (1987). Four different forms of interferon-induced 2′,5′-oligo(A) synthetase identified by immunoblotting in human cells. J. Biol. Chem. *262*, 3852–3857. https://doi.org/10.1016/S0021-9258(18)61434-6.

36. Hartmann, R., Justesen, J., Sarkar, S.N., Sen, G.C., and Yee, V.C. (2003). Crystal structure of the 2′-specific and double-stranded RNA-activated interferon-induced antiviral protein 2′-5′-oligoadenylate synthetase. Mol. Cell *12*, 1173–1185. https://doi.org/10.1016/s1097-2765(03)00433-7.

37. Lohöfener, J., Steinke, N., Kay-Fedorov, P., Baruch, P., Nikulin, A., Tishchenko, S., Manstein, D.J., and Fedorov, R. (2015). The activation mechanism of 2′-5′-oligoadenylate synthetase gives new insights into OAS/cGAS triggers of innate immunity. Structure *23*, 851–862. https://doi.org/10.1016/j.str.2015.03.012.

38. Donovan, J., Dufner, M., and Korennykh, A. (2013). Structural basis for cytosolic double-stranded RNA surveillance by human oligoadenylate synthetase 1. Proc. Natl. Acad. Sci. USA. *110*, 1652–1657. https://doi.org/10.1073/pnas.1218528110.

39. Hovnanian, A., Rebouillat, D., Mattei, M.G., Levy, E.R., Marié, I., Monaco, A.P., and Hovanessian, A.G. (1998). The human 2′,5′-oligoadenylate synthetase locus is composed of three distinct genes clustered on chromosome 12q24.2 encoding the 100-, 69-, and 40-kDa forms. Genomics *52*, 267–277. https://doi.org/10.1006/geno.1998.5443.

40. Sarkar, S.N., Miyagi, M., Crabb, J.W., and Sen, G.C. (2002). Identification of the substrate-binding sites of 2′-5′-oligoadenylate synthetase. J. Biol. Chem. *277*, 24321–24330. https://doi.org/10.1074/jbc.M110202200.

41. Sarkar, S.N., Pal, S., and Sen, G.C. (2002). Crisscross enzymatic reaction between the two molecules in the active dimeric P69 form of the 2′-5′ oligodenylate synthetase. J. Biol. Chem. *277*, 44760–44764. https://doi.org/10.1074/jbc.M207126200.

42. Hu, J., Wang, X., Xing, Y., Rong, E., Ning, M., Smith, J., and Huang, Y. (2018). Origin and development of oligoadenylate synthetase immune system. BMC Evol. Biol. *18*, 201. https://doi.org/10.1186/s12862-018-1315-x.

43. Rogozin, I.B., Aravind, L., and Koonin, E.V. (2003). Differential Action of Natural Selection on the N and C-terminal Domains of 2′-5′ Oligoadenylate Synthetases and the Potential Nuclease Function of the C-terminal Domain. J. Mol. Biol. *326*, 1449–1461. https://doi.org/10.1016/S0022-2836(03)00055-X.

44. Sarkar, S.N., Ghosh, A., Wang, H.W., Sung, S.S., and Sen, G.C. (1999). The nature of the catalytic domain of 2′-5′-oligoadenylate synthetases. J. Biol. Chem. *274*, 25535–25542. https://doi.org/10.1074/jbc.274.36.25535.

45. Donovan, J., Whitney, G., Rath, S., and Korennykh, A. (2015). Structural mechanism of sensing long dsRNA via a noncatalytic domain in human oligoadenylate synthetase 3. Proc. Natl. Acad. Sci. USA. *112*, 3949–3954. https://doi.org/10.1073/pnas.1419409112.

46. Koul, A., Gemmill, D., Lubna, N., Meier, M., Krahn, N., Booy, E.P., Stetefeld, J., Patel, T.R., and McKenna, S.A. (2020). Structural and Hydrodynamic Characterization of Dimeric Human Oligoadenylate Synthetase 2. Biophys. J. *118*, 2726–2740. https://doi.org/10.1016/j.bpj.2020.04.025.

47. Koul, A., Deo, S., Booy, E.P., Orriss, G.L., Genung, M., and McKenna, S.A. (2020). Impact of double-stranded RNA characteristics on the activation of human 2′-5′-oligoadenylate synthetase 2 (OAS2). Biochem. Cell Biol. *98*, 70–82. https://doi.org/10.1139/bcb-2019-0060.

48. Marié, I., Rebouillat, D., and Hovanessian, A.G. (1999). The expression of both domains of the 69/71 kDa 2′,5′ oligoadenylate synthetase generates a catalytically active enzyme and mediates an anti-viral response. Eur. J. Biochem. *262*, 155–165. https://doi.org/10.1046/j.1432-1327.1999.00361.x.

49. Wang, Y., Holleufer, A., Gad, H.H., and Hartmann, R. (2020). Length dependent activation of OAS proteins by dsRNA. Cytokine *126*, 154867. https://doi.org/10.1016/j.cyto.2019.154867.

50. El Awady, M.K., Anany, M.A., Esmat, G., Zayed, N., Tabll, A.A., Helmy, A., El Zayady, A.R., Abdalla, M.S., Sharada, H.M., El Raziky, M., et al. (2011). Single nucleotide polymorphism at exon 7 splice acceptor site of OAS1 gene determines response of hepatitis C virus patients to interferon therapy. J. Gastroenterol. Hepatol. *26*, 843–850. https://doi.org/10.1111/j.1440-1746.2010.06605.x.

51. Lin, R.J., Yu, H.P., Chang, B.L., Tang, W.C., Liao, C.L., and Lin, Y.L. (2009). Distinct antiviral roles for human 2′,5′-oligoadenylate synthetase family members against dengue virus infection. J. Immunol. *183*, 8035–8043. https://doi.org/10.4049/jimmunol.0902728.

52. Li, Y., Banerjee, S., Wang, Y., Goldstein, S.A., Dong, B., Gaughan, C., Silverman, R.H., and Weiss, S.R. (2016). Activation of RNase L is dependent on OAS3 expression during infection with diverse human viruses. Proc. Natl. Acad. Sci. USA. *113*, 2241–2246. https://doi.org/10.1073/pnas.1519657113.

53. Harioudh, M.K., Perez, J., Chong, Z., Nair, S., So, L., McCormick, K.D., Ghosh, A., Shao, L., Srivastava, R., Soveg, F., et al. (2024). Oligoadenylate synthetase 1 displays dual antiviral mechanisms in driving translational shutdown and protecting interferon production. S1074761324000773. Immunity *57*, 446–461.e7. https://doi.org/10.1016/j.immuni.2024.02.002.

54. Marié, I., Svab, J., Robert, N., Galabru, J., and Hovanessian, A.G. (1990). Differential expression and distinct structure of 69- and 100-kDa forms of 2–5A synthetase in human cells treated with interferon. J. Biol. Chem. *265*, 18601–18607. https://doi.org/10.1016/s0021-9258(17)44794-6.

55. Kondratova, A.A., Cheon, H., Dong, B., Holvey-Bates, E.G., Hasipek, M., Taran, I., Gaughan, C., Jha, B.K., Silverman, R.H., and Stark, G.R. (2020). Suppressing PARylation by 2′,5′-oligoadenylate synthetase 1 inhibits DNA damage-induced cell death. EMBO J. *39*, e101573. https://doi.org/10.15252/embj.2019101573.

56. Ghosh, A., Sarkar, S.N., Guo, W., Bandyopadhyay, S., and Sen, G.C. (1997). Enzymatic activity of 2′-5′-oligoadenylate synthetase is impaired by specific mutations that affect oligomerization of the protein. J. Biol. Chem. *272*, 33220–33226. https://doi.org/10.1074/jbc.272.52.33220.

57. Ibsen, M.S., Gad, H.H., Andersen, L.L., Hornung, V., Julkunen, I., Sarkar, S.N., and Hartmann, R. (2015). Structural and functional analysis reveals that human OASL binds dsRNA to enhance RIG-I signaling. Nucleic Acids Res. *43*, 5236–5248. https://doi.org/10.1093/nar/gkv389.

58. Balbo, P.B., and Bohm, A. (2007). Mechanism of Poly(A) Polymerase: Structure of the Enzyme-MgATP-RNA Ternary Complex and Kinetic Analysis. Structure *15*, 1117–1131. https://doi.org/10.1016/j.str.2007.07.010.

59. Abramson, J., Adler, J., Dunger, J., Evans, R., Green, T., Pritzel, A., Ronneberger, O., Willmore, L., Ballard, A.J., Bambrick, J., et al. (2024). Accurate structure prediction of biomolecular interactions with AlphaFold 3. Nature *630*, 493–500. https://doi.org/10.1038/s41586-024-07487-w.

60. Schwartz, S.L., and Conn, G.L. (2019). RNA regulation of the antiviral protein 2′-5′-oligoadenylate synthetase. Wiley Interdiscip. Rev. RNA *10*, e1534. https://doi.org/10.1002/wrna.1534.

61. Desai, S.Y., and Sen, G.C. (1997). Effects of varying lengths of double-stranded RNA on binding and activation of 2′-5′-oligoadenylate synthetase. J. Interferon Cytokine Res. *17*, 531–536. https://doi.org/10.1089/jir.1997.17.531.

62. Chitrakar, A., Rath, S., Donovan, J., Demarest, K., Li, Y., Sridhar, R.R., Weiss, S.R., Kotenko, S.V., Wingreen, N.S., and Korennykh, A. (2019). Real-time 2–5A kinetics suggest that interferons beta and lambda evade global arrest of translation by RNase L. Proc. Natl. Acad. Sci. USA. *116*, 2103–2111. https://doi.org/10.1073/pnas.1818363116.

Please cite this article in press as: Merold et al., Structural basis for OAS2 regulation and its antiviral function, Molecular Cell (2025), https://doi.org/10.1016/j.molcel.2025.05.001

63. Rebouillat, D., Hovnanian, A., Marié, I., and Hovanessian, A.G. (1999). The 100-kDa 2′,5′-Oligoadenylate Synthetase Catalyzing Preferentially the Synthesis of Dimeric pppA2′p5′A Molecules Is Composed of Three Homologous Domains. J. Biol. Chem. *274*, 1557–1565. https://doi.org/10.1074/jbc.274.3.1557.

64. Marié, I., Blanco, J., Rebouillat, D., and Hovanessian, A.G. (1997). 69-kDa and 100-kDa Isoforms of Interferon-Induced (2'-5')Oligoadenylate Synthetase Exhibit Differential Catalytic Parameters. Eur. J. Biochem. *248*, 558–566. https://doi.org/10.1111/j.1432-1033.1997.t01-1-00558.x.

65. Ibsen, M.S., Gad, H.H., Thavachelvam, K., Boesen, T., Desprès, P., and Hartmann, R. (2014). The 2'-5′-oligoadenylate synthetase 3 enzyme potently synthesizes the 2'-5′-oligoadenylates required for RNase L activation. J. Virol. *88*, 14222–14231. https://doi.org/10.1128/JVI.01763-14.

66. Hartmann, R., Norby, P.L., Martensen, P.M., Jorgensen, P., James, M.C., Jacobsen, C., Moestrup, S.K., Clemens, M.J., and Justesen, J. (1998). Activation of 2'-5′ oligoadenylate synthetase by single-stranded and double-stranded RNA aptamers. J. Biol. Chem. *273*, 3236–3246. https://doi.org/10.1074/jbc.273.6.3236.

67. Kodym, R., Kodym, E., and Story, M.D. (2009). 2'-5′-Oligoadenylate synthetase is activated by a specific RNA sequence motif. Biochem. Biophys. Res. Commun. *388*, 317–322. https://doi.org/10.1016/j.bbrc.2009.07.167.

68. Schwartz, S.L., Park, E.N., Vachon, V.K., Danzy, S., Lowen, A.C., and Conn, G.L. (2020). Human OAS1 activation is highly dependent on both RNA sequence and context of activating RNA motifs. Nucleic Acids Res. *48*, 7520–7531. https://doi.org/10.1093/nar/gkaa513.

69. Schwartz, S.L., Dey, D., Tanquary, J., Bair, C.R., Lowen, A.C., and Conn, G.L. (2022). Role of helical structure and dynamics in oligoadenylate synthetase 1 (OAS1) mismatch tolerance and activation by short dsRNAs. Proc. Natl. Acad. Sci. USA. *119*, e2107111119. https://doi.org/10.1073/pnas.2107111119.

70. Nakamura, N., Rabouille, C., Watson, R., Nilsson, T., Hui, N., Slusarewicz, P., Kreis, T.E., and Warren, G. (1995). Characterization of a cis-Golgi matrix protein, GM130. J. Cell Biol. *131*, 1715–1726. https://doi.org/10.1083/jcb.131.6.1715.

71. Tie, H.C., Mahajan, D., Chen, B., Cheng, L., VanDongen, A.M.J., and Lu, L. (2016). A novel imaging method for quantitative Golgi localization reveals differential intra-Golgi trafficking of secretory cargoes. Mol. Biol. Cell *27*, 848–861. https://doi.org/10.1091/mbc.E15-09-0664.

72. Cole, N.B., Smith, C.L., Sciaky, N., Terasaki, M., Edidin, M., and Lippincott-Schwartz, J. (1996). Diffusional mobility of Golgi proteins in membranes of living cells. Science *273*, 797–801. https://doi.org/10.1126/science.273.5276.797.

73. Harioudh, M.K., Perez, J., So, L., Maheshwari, M., Ebert, T.S., Hornung, V., Savan, R., Rouf Banday, A., Diamond, M.S., Rathinam, V.A., et al. (2024). The canonical antiviral protein oligoadenylate synthetase 1 elicits antibacterial functions by enhancing IRF1 translation. Immunity *57*, 1812–1827.e7. https://doi.org/10.1016/j.immuni.2024.06.003.

74. Bréhin, A.-C., Casadémont, I., Frenkiel, M.-P., Julier, C., Sakuntabhai, A., and Desprès, P. (2009). The large form of human 2′,5′-Oligoadenylate Synthetase (OAS3) exerts antiviral effect against Chikungunya virus. Virology *384*, 216–222. https://doi.org/10.1016/j.virol.2008.10.021.

75. Odon, V., Fros, J.J., Goonawardane, N., Dietrich, I., Ibrahim, A., Alshaikhahmed, K., Nguyen, D., and Simmonds, P. (2019). The role of ZAP and OAS3/RNAseL pathways in the attenuation of an RNA virus with elevated frequencies of CpG and UpA dinucleotides. Nucleic Acids Res. *47*, 8061–8083. https://doi.org/10.1093/nar/gkz581.

76. Cusic, R., and Burke, J.M. (2024). Condensation of RNase L promotes its rapid activation in response to viral infection in mammalian cells. Sci. Signal. *17*, eadi9844. https://doi.org/10.1126/scisignal.adi9844.

77. Paul, D., and Bartenschlager, R. (2013). Architecture and biogenesis of plus-strand RNA virus replication factories. World J. Virol. *2*, 32–48. https://doi.org/10.5501/wjv.v2.i2.32.

78. Meng, H., Deo, S., Xiong, S., Dzananovic, E., Donald, L.J., Van Dijk, C.W., and McKenna, S.A. (2012). Regulation of the interferon-inducible 2′-5′-oligoadenylate synthetases by adenovirus VAI RNA. J. Mol. Biol. *422*, 635–649. https://doi.org/10.1016/j.jmb.2012.06.017.

79. Maitra, R.K., McMillan, N.A.J., Desai, S., McSwiggen, J., Hovanessian, A.G., Sen, G., Williams, B.R.G., and Silverman, R.H. (1994). HIV-1 TAR RNA Has an Intrinsic Ability to Activate Interferon-Inducible Enzymes. Virology *204*, 823–827. https://doi.org/10.1006/viro.1994.1601.

80. Deo, S., Patel, T.R., Dzananovic, E., Booy, E.P., Zeid, K., McEleney, K., Harding, S.E., and McKenna, S.A. (2014). Activation of 2′ 5′-oligoadenylate synthetase by stem loops at the 5′-end of the west nile virus genome. PLoS One *9*, e92545. https://doi.org/10.1371/journal.pone.0092545.

81. Sharp, T.V., Raine, D.A., Gewert, D.R., Joshi, B., Jagus, R., and Clemens, M.J. (1999). Activation of the Interferon-Inducible (2′-5′) Oligoadenylate Synthetase by the Epstein–Barr Virus RNA, EBER-1. Virology *257*, 303–313. https://doi.org/10.1006/viro.1999.9689.

82. Mordechai, E., Kon, N., Henderson, E.E., and Suhadolnik, R.J. (1995). Activation of the Interferon-Inducible Enzymes, 2′, 5′-Oligoadenylate Synthetase and PKR by Human T-Cell Leukemia Virus Type I Rex-Response Element. Virology *206*, 913–922. https://doi.org/10.1006/viro.1995.1014.

83. Desai, S.Y., Patel, R.C., Sen, G.C., Malhotra, P., Ghadge, G.D., and Thimmapaya, B. (1995). Activation of Interferon-inducible 2′−5′ Oligoadenylate Synthetase by Adenoviral VAI RNA. J. Biol. Chem. *270*, 3454–3461. https://doi.org/10.1074/jbc.270.7.3454.

84. Drappier, M., and Michiels, T. (2015). Inhibition of the OAS/RNase L pathway by viruses. Curr. Opin. Virol. *15*, 19–26. https://doi.org/10.1016/j.coviro.2015.07.002.

85. Pichlmair, A., Schulz, O., Tan, C.-P., Rehwinkel, J., Kato, H., Takeuchi, O., Akira, S., Way, M., Schiavo, G., and Reis e Sousa, C.R.e. (2009). Activation of MDA5 Requires Higher-Order RNA Structures Generated during Virus Infection. J. Virol. *83*, 10761–10769. https://doi.org/10.1128/JVI.00770-09.

86. Haas, D.A., Meiler, A., Geiger, K., Vogt, C., Preuss, E., Kochs, G., and Pichlmair, A. (2018). Viral targeting of TFIIB impairs de novo polymerase II recruitment and affects antiviral immunity. PLoS Pathog. *14*, e1006980. https://doi.org/10.1371/journal.ppat.1006980.

87. Pichlmair, A., Lassnig, C., Eberle, C.-A., Górna, M.W., Baumann, C.L., Burkard, T.R., Bürckstümmer, T., Stefanovic, A., Krieger, S., Bennett, K.L., et al. (2011). IFIT1 is an antiviral protein that recognizes 5′-triphosphate RNA. Nat. Immunol. *12*, 624–630. https://doi.org/10.1038/ni.2048.

88. Santos-Peral, A., Luppa, F., Goresch, S., Nikolova, E., Zaucha, M., Lehmann, L., Dahlstroem, F., Karimzadeh, H., Thorn-Seshold, J., Winheim, E., et al. (2024). Prior flavivirus immunity skews the yellow fever vaccine response to cross-reactive antibodies with potential to enhance dengue virus infection. Nat. Commun. *15*, 1696. https://doi.org/10.1038/s41467-024-45806-x.

89. Scaturro, P., Stukalov, A., Haas, D.A., Cortese, M., Draganova, K., Płaszczyca, A., Bartenschlager, R., Götz, M., and Pichlmair, A. (2018). An orthogonal proteomic survey uncovers novel Zika virus host factors. Nature *561*, 253–257. https://doi.org/10.1038/s41586-018-0484-5.

90. Habjan, M., Penski, N., Spiegel, M., and Weber, F. (2008). T7 RNA polymerase-dependent and -independent systems for cDNA-based rescue of Rift Valley fever virus. J. Gen. Virol. *89*, 2157–2166. https://doi.org/10.1099/vir.0.2008/002097-0.

91. Huang, Y., Bergant, V., Grass, V., Emslander, Q., Hamad, M.S., Hubel, P., Mergner, J., Piras, A., Krey, K., Henrici, A., et al. (2024). Multi-omics characterization of the monkeypox virus infection. Nat. Commun. *15*, 6778. https://doi.org/10.1038/s41467-024-51074-6.

Please cite this article in press as: Merold et al., Structural basis for OAS2 regulation and its antiviral function, Molecular Cell (2025), https://doi.org/10.1016/j.molcel.2025.05.001

92. Stringer, B.W., Day, B.W., D'Souza, R.C.J., Jamieson, P.R., Ensbey, K. S., Bruce, Z.C., Lim, Y.C., Goasdoué, K., Offenhäuser, C., Akgül, S., et al. (2019). A reference collection of patient-derived cell line and xenograft models of proneural, classical and mesenchymal glioblastoma. Sci. Rep. *9*, 4902. https://doi.org/10.1038/s41598-019-41277-z.

93. Campeau, E., Ruhl, V.E., Rodier, F., Smith, C.L., Rahmberg, B.L., Fuss, J. O., Campisi, J., Yaswen, P., Cooper, P.K., and Kaufman, P.D. (2009). A versatile viral system for expression and depletion of proteins in mammalian cells. PLoS One *4*, e6529. https://doi.org/10.1371/journal.pone.0006529.

94. Xie, Q., Bozzo, C.P., Eiben, L., Noettger, S., Kmiec, D., Nchioua, R., Niemeyer, D., Volcic, M., Lee, J.-H., Zech, F., et al. (2023). Endogenous IFITMs boost SARS-coronavirus 1 and 2 replication whereas overexpression inhibits infection by relocalizing ACE2. iScience *26*, 106395. https://doi.org/10.1016/j.isci.2023.106395.

95. Greenberg, M.E., Iafrate, A.J., and Skowronski, J. (1998). The SH3 domain-binding surface and an acidic motif in HIV-1 Nef regulate trafficking of class I MHC complexes. EMBO J. *17*, 2777–2789. https://doi.org/10.1093/emboj/17.10.2777.

96. Pettersen, E.F., Goddard, T.D., Huang, C.C., Meng, E.C., Couch, G.S., Croll, T.I., Morris, J.H., and Ferrin, T.E. (2021). UCSF ChimeraX: Structure visualization for researchers, educators, and developers. Protein Sci. *30*, 70–82. https://doi.org/10.1002/pro.3943.

97. Punjani, A., Rubinstein, J.L., Fleet, D.J., and Brubaker, M.A. (2017). cryoSPARC: algorithms for rapid unsupervised cryo-EM structure determination. Nat. Methods *14*, 290–296. https://doi.org/10.1038/nmeth.4169.

98. Emsley, P., and Cowtan, K. (2004). Coot: model-building tools for molecular graphics. Acta Crystallogr. D *60*, 2126–2132. https://doi.org/10.1107/S0907444904019158.

99. Adams, P.D., Afonine, P.V., Bunkóczi, G., Chen, V.B., Davis, I.W., Echols, N., Headd, J.J., Hung, L.W., Kapral, G.J., Grosse-Kunstleve, R.W., et al. (2010). PHENIX: a comprehensive Python-based system for macromolecular structure solution. Acta Crystallogr. D *66*, 213–221. https://doi.org/10.1107/S0907444909052925.

100. Bepler, T., Morin, A., Rapp, M., Brasch, J., Shapiro, L., Noble, A.J., and Berger, B. (2019). Positive-unlabeled convolutional neural networks for particle picking in cryo-electron micrographs. Nat. Methods *16*, 1153–1160. https://doi.org/10.1038/s41592-019-0575-8.

101. Crooks, G.E., Hon, G., Chandonia, J.M., and Brenner, S.E. (2004). WebLogo: a sequence logo generator. Genome Res. *14*, 1188–1190. https://doi.org/10.1101/gr.849004.

102. Katoh, K., Rozewicki, J., and Yamada, K.D. (2019). MAFFT online service: multiple sequence alignment, interactive sequence choice and visualization. Brief. Bioinform. *20*, 1160–1166. https://doi.org/10.1093/bib/bbx108.

103. Waterhouse, A.M., Procter, J.B., Martin, D.M., Clamp, M., and Barton, G. J. (2009). Jalview, [Version 2]–a multiple sequence alignment editor and analysis workbench. Bioinformatics *25*, 1189–1191. https://doi.org/10.1093/bioinformatics/btp033.

104. Abraham, M.J., Murtola, T., Schulz, R., Páll, S., Smith, J.C., Hess, B., and Lindahl, E. (2015). GROMACS: High performance molecular simulations through multi-level parallelism from laptops to supercomputers. SoftwareX *1–2*, 19–25. https://doi.org/10.1016/j.softx.2015.06.001.

105. Case, D.A., Aktulga, H.M., Belfon, K., Cerutti, D.S., Cisneros, G.A., Cruzeiro, V.W.D., Forouzesh, N., Giese, T.J., Götz, A.W., Gohlke, H., et al. (2023). AmberTools. J. Chem. Inf. Model. *63*, 6183–6191. https://doi.org/10.1021/acs.jcim.3c01153.

106. Jurrus, E., Engel, D., Star, K., Monson, K., Brandi, J., Felberg, L.E., Brookes, D.H., Wilson, L., Chen, J., Liles, K., et al. (2018). Improvements to the APBS biomolecular solvation software suite. Protein Sci. *27*, 112–128. https://doi.org/10.1002/pro.3280.

107. Michaud-Agrawal, N., Denning, E.J., Woolf, T.B., and Beckstein, O. (2011). MDAnalysis: A toolkit for the analysis of molecular dynamics simulations. J. Comput. Chem. *32*, 2319–2327. https://doi.org/10.1002/jcc.21787.

108. Gowers, R.J., Linke, M., Barnoud, J., Reddy, T.J.E., Melo, M.N., Seyler, S.L., Domański, J., Dotson, D.L., Buchoux, S., Kenney, I.M., et al. (2016). MDAnalysis: A Python Package for the Rapid Analysis of Molecular Dynamics Simulations. Proceedings of the Python in Science Conference *qq*, 98–105. https://doi.org/10.25080/Majora-629e541a-00e.

109. Roet, S., Hooft, F., Bolhuis, P.G., Swenson, D.W.H., and Vreede, J. (2022). Path Sampling Simulations Reveal How the Q61L Mutation Alters the Dynamics of KRas. J. Phys. Chem. B *126*, 10034–10044. https://doi.org/10.1021/acs.jpcb.2c06235.

110. Schindelin, J., Arganda-Carreras, I., Frise, E., Kaynig, V., Longair, M., Pietzsch, T., Preibisch, S., Rueden, C., Saalfeld, S., Schmid, B., et al. (2012). Fiji: an open-source platform for biological-image analysis. Nat. Methods *9*, 676–682. https://doi.org/10.1038/nmeth.2019.

111. Patro, R., Duggal, G., Love, M.I., Irizarry, R.A., and Kingsford, C. (2017). Salmon provides fast and bias-aware quantification of transcript expression. Nat. Methods *14*, 417–419. https://doi.org/10.1038/nmeth.4197.

112. Soneson, C., Love, M.I., and Robinson, M.D. (2015). Differential analyses for RNA-seq: transcript-level estimates improve gene-level inferences. F1000Res *4*, 1521. https://doi.org/10.12688/f1000research.7563.2.

113. Love, M.I., Huber, W., and Anders, S. (2014). Moderated estimation of fold change and dispersion for RNA-seq data with DESeq2. Genome Biol. *15*, 550. https://doi.org/10.1186/s13059-014-0550-8.

114. Ritchie, M.E., Phipson, B., Wu, D., Hu, Y., Law, C.W., Shi, W., and Smyth, G.K. (2015). limma powers differential expression analyses for RNA-sequencing and microarray studies. Nucleic Acids Res. *43*, e47. https://doi.org/10.1093/nar/gkv007.

115. Wickham, H. (2016). (ggplot2: Elegant Graphics for Data Analysis) (Springer-Verlag New York).

116. Cox, J., and Mann, M. (2008). MaxQuant enables high peptide identification rates, individualized p.p.b.-range mass accuracies and proteome-wide protein quantification. Nat. Biotechnol. *26*, 1367–1372. https://doi.org/10.1038/nbt.1511.

117. Tyanova, S., Temu, T., and Cox, J. (2016). The MaxQuant computational platform for mass spectrometry-based shotgun proteomics. Nat. Protoc. *11*, 2301–2319. https://doi.org/10.1038/nprot.2016.136.

118. MacLean, B., Tomazela, D.M., Shulman, N., Chambers, M., Finney, G.L., Frewen, B., Kern, R., Tabb, D.L., Liebler, D.C., and MacCoss, M.J. (2010). Skyline: an open source document editor for creating and analyzing targeted proteomics experiments. Bioinformatics *26*, 966–968. https://doi.org/10.1093/bioinformatics/btq054.

119. Boehmer, D.F.R., Formisano, S., de Oliveira Mann, C.C., Mueller, S.A., Kluge, M., Metzger, P., Rohlfs, M., Hörth, C., Kocheise, L., Lichtenthaler, S.F., et al. (2021). OAS1/RNase L executes RIG-I ligand-dependent tumor cell apoptosis. Sci. Immunol. *6*, eabe2550. https://doi.org/10.1126/sciimmunol.abe2550.

120. Zheng, S.Q., Palovcak, E., Armache, J.P., Verba, K.A., Cheng, Y., and Agard, D.A. (2017). MotionCor2: anisotropic correction of beam-induced motion for improved cryo-electron microscopy. Nat. Methods *14*, 331–332. https://doi.org/10.1038/nmeth.4193.

121. Rohou, A., and Grigorieff, N. (2015). CTFFIND4: Fast and accurate defocus estimation from electron micrographs. J. Struct. Biol. *192*, 216–221. https://doi.org/10.1016/j.jsb.2015.08.008.

122. Meng, E.C., Goddard, T.D., Pettersen, E.F., Couch, G.S., Pearson, Z.J., Morris, J.H., and Ferrin, T.E. (2023). UCSF ChimeraX: Tools for structure building and analysis. Protein Sci. *32*, e4792. https://doi.org/10.1002/pro.4792.

Please cite this article in press as: Merold et al., Structural basis for OAS2 regulation and its antiviral function, Molecular Cell (2025), https://doi.org/10.1016/j.molcel.2025.05.001

123. Tian, C., Kasavajhala, K., Belfon, K.A.A., Raguette, L., Huang, H., Migues, A.N., Bickel, J., Wang, Y., Pincay, J., Wu, Q., et al. (2020). ff19SB: Amino-Acid-Specific Protein Backbone Parameters Trained against Quantum Mechanics Energy Surfaces in Solution. J. Chem. Theor. Comput. *16*, 528–552. https://doi.org/10.1021/acs.jctc.9b00591.

124. Izadi, S., Anandakrishnan, R., and Onufriev, A.V. (2014). Building Water Models: A Different Approach. J. Phys. Chem. Lett. *5*, 3863–3871. https://doi.org/10.1021/jz501780a.

125. Mamatkulov, S., and Schwierz, N. (2018). Force fields for monovalent and divalent metal cations in TIP3P water based on thermodynamic and kinetic properties. J. Chem. Phys. *148*, 074504. https://doi.org/10.1063/1.5017694.

126. Li, Z., Song, L.F., Li, P., and Merz, K.M., Jr. (2020). Systematic Parametrization of Divalent Metal Ions for the OPC3, OPC, TIP3P-FB, and TIP4P-FB Water Models. J. Chem. Theor. Comput. *16*, 4429–4442. https://doi.org/10.1021/acs.jctc.0c00194.

127. Bussi, G., Donadio, D., and Parrinello, M. (2007). Canonical sampling through velocity rescaling. J. Chem. Phys. *126*, 014101. https://doi.org/10.1063/1.2408420.

128. Parrinello, M., and Rahman, A. (1981). Polymorphic transitions in single crystals: A new molecular dynamics method. J. Appl. Phys. *52*, 7182–7190. https://doi.org/10.1063/1.328693.

129. Wang, J., Cieplak, P., and Kollman, P.A. (2000). How well does a restrained electrostatic potential (RESP) model perform in calculating conformational energies of organic and biological molecules? J. Comput. Chem. *21*, 1049–1074. https://doi.org/10.1002/1096-987X(200009)21:12<1049::AID-JCC3>3.0.CO;2-F.

130. Pérez, A., Marchán, I., Svozil, D., Sponer, J., Cheatham, T.E., 3rd, Laughton, C.A., and Orozco, M. (2007). Refinement of the AMBER force field for nucleic acids: improving the description of alpha/gamma conformers. Biophys. J. *92*, 3817–3829. https://doi.org/10.1529/biophysj.106.097782.

131. Zgarbová, M., Otyepka, M., Šponer, J., Mládek, A., Banáš, P., Cheatham, T.E., III, and Jurečka, P. (2011). Refinement of the Cornell et al. Nucleic Acids Force Field Based on Reference Quantum Chemical Calculations of Glycosidic Torsion Profiles. J. Chem. Theor. Comput. *7*, 2886–2902. https://doi.org/10.1021/ct200162x.

132. Hess, B., Bekker, H., Berendsen, H.J.C., and Fraaije, J.G.E.M. (1997). LINCS: A linear constraint solver for molecular simulations. J. Comput. Chem. *18*, 1463–1472. https://doi.org/10.1002/(SICI)1096-987X(199709)18:12<1463::AID-JCC4>3.0.CO;2-H.

133. Berendsen, H.J.C., Postma, J.P.M., van Gunsteren, W.F., DiNola, A., and Haak, J.R. (1984). Molecular dynamics with coupling to an external bath. J. Chem. Phys. *81*, 3684–3690. https://doi.org/10.1063/1.448118.

134. McGibbon, R.T., Beauchamp, K.A., Harrigan, M.P., Klein, C., Swails, J. M., Hernández, C.X., Schwantes, C.R., Wang, L.-P., Lane, T.J., and Pande, V.S. (2015). MDTraj: A Modern Open Library for the Analysis of Molecular Dynamics Trajectories. Biophys. J. *109*, 1528–1532. https://doi.org/10.1016/j.bpj.2015.08.015.

135. Sanjana, N.E., Shalem, O., and Zhang, F. (2014). Improved vectors and genome-wide libraries for CRISPR screening. Nat. Methods *11*, 783–784. https://doi.org/10.1038/nmeth.3047.

136. Law, C.W., Chen, Y., Shi, W., and Smyth, G.K. (2014). voom: precision weights unlock linear model analysis tools for RNA-seq read counts. Genome Biol. *15*, R29. https://doi.org/10.1186/gb-2014-15-2-r29.

137. Huang da, W., Sherman, B.T., and Lempicki, R.A. (2009). Systematic and integrative analysis of large gene lists using DAVID bioinformatics resources. Nat. Protoc. *4*, 44–57. https://doi.org/10.1038/nprot.2008.211.

138. Shevchenko, A., Tomas, H., Havlis, J., Olsen, J.V., and Mann, M. (2006). In-gel digestion for mass spectrometric characterization of proteins and proteomes. Nat. Protoc. *1*, 2856–2860. https://doi.org/10.1038/nprot.2006.468.

Please cite this article in press as: Merold et al., Structural basis for OAS2 regulation and its antiviral function, Molecular Cell (2025), https://doi.org/10.1016/j.molcel.2025.05.001

CellPress
OPEN ACCESS

STAR★METHODS

KEY RESOURCES TABLE

REAGENT or RESOURCE	SOURCE	IDENTIFIER
Antibodies		
anti-OAS2	R&D Systems	Cat#MAB1925-SP; RRID:AB_215616
anti-OAS2	Proteintech	Cat#19279-1-AP, lot# 00113570; RRID:AB_10642832
anti-OAS1	Cell Signaling	Cat#14498S; RRID:AB_2798498
anti-GM130	Thermo Fisher Scientific	Cat#703794; RRID:AB_2848241
anti-GM130	Proteintech	Cat#66662-1-Ig; RRID:AB_2882017
anti-calnexin	R&D Systems	Cat#NB100-1965SS; RRID:AB_10002123
anti-giantin	R&D Systems	Cat#NBP1-91937; RRID:AB_11024007
anti-TGN46	R&D Systems	Cat#NBP1-49643SS; RRID:AB_10011761
anti-Golgi 58K	Sigma-Aldrich	Cat#G2404; RRID: AB_477002
anti-dsRNA J2	SCICONS	Cat#1qq0010500; RRID: AB_2651015
anti-OAS3	Proteintech	Cat#21915-1-AP RRID:AB_2876880
anti-GAPDH	Santa cruz	Cat#sc-47724; RRID:AB_627678
anti-FLAG-M2-HRP	Sigma Aldrich	Cat#A8592; RRID:AB_439702
anti-RNase L	Santa cruz	Cat#sc-74405; RRID:AB_2181661
anti-OAS1	Proteintech	Cat#14955-1-AP; RRID:AB_2158292
anti-GFP	Abcam	Cat# ab290; RRID: AB_2313768
anti-mouse AF488	Invitrogen	Cat#A11029; RRID: AB_2534088
anti-rabbit AF647	Thermo Fisher	Cat#A31573; RRID: AB_2536183
anti-rabbit AF488	Cell Signaling	Cat#4412S; RRID: AB_1904025
anti-mouse AF647	Thermo Fisher	Cat#A31571; RRID: AB_162542
anti-rabbit AF488	Invitrogen	Cat# A-11008; RRID: AB_143165
Anti-mouse AF594	Invitrogen	Cat#A11032; RRID: AB_2534091
Bacterial and virus strains		
E. coli Rosetta	Expression Systems	N/A
E. coli STBL3	Andreas Pichlmair	N/A
E. coli DH5alpha	Andreas Pichlmair	N/A
E. coli DH10alphaMultiBac	Expression Systems	N/A
BUNV wt	Friedemann Weber	N/A
EMCV	Andreas Pichlmair, Pichlmair et al.[85]	N/A
HSV1(17+)Lox-GFP	Beate Sodeik	N/A
LACV (rec wt)	Friedemann Weber	N/A
THOV-ML$^-$	Andreas Pichlmair, Haas et al.[86]	N/A
VACV-V300-GFP	Joachim Bugert	N/A
VSV-AV3-GFP (Indiana)	Andreas Pichlmair lab, Pichlmair et al.[87]	N/A
YFV (YF-17D)-Venus	Simon Rothenfußer, Santos-Peral et al.[88]	N/A
YFV (YF-17D)	Simon Rothenfußer, Santos-Peral et al.[88]	N/A
ZIKV H/PF/2013	Andreas Pichlmair lab, Scaturro et al.[89]	N/A
IAV SC35M PB2 2A GFP	Martin Schwemmle	N/A
RVFV-GFP	Friedemann Weber, Habjan et al.[90]	N/A
HRV16	ATCC	Cat# VR-283
HCoV-OC43	ATCC	Cat# CR-1558TM
NL63	Lia van der Hoek	N/A

(*Continued on next page*)

Please cite this article in press as: Merold et al., Structural basis for OAS2 regulation and its antiviral function, Molecular Cell (2025), https://doi.org/10.1016/j.molcel.2025.05.001

Continued

REAGENT or RESOURCE	SOURCE	IDENTIFIER
SARS-CoV-2 (strain Netherlands/01/NL/2020)	European Virus Archive	Cat# 010V 03903
Biological samples		
Patient fibroblasts (primary human fibroblasts)	This paper	N/A
WT fibroblasts (primary human fibroblasts)	This paper	N/A
Chemicals, peptides, and recombinant proteins		
Ni-NTA Agarose	Macherey Nagel	Cat#745400.100
Ammonium molybdate	Sigma Aldrich	Cat#277908
ATP	Sigma Aldrich	Cat#11140965001
β-Octylglycoside	Sigma Aldrich	Cat#O8001
Poly I:C	Sigma Aldrich	Cat#P9582
Lipofectamine2000	Thermo Fisher	Cat#11668019
Lipofectamine3000	Thermo Fisher	Cat#L3000015
Pyrophosphate	VWR	J62052.AE
IFN-alpha B/D	Prof. Dr. Peter Stäheli	N/A
IFN-Beta	R&D systems	Cat# 8499-IF-010
IFN-Alpha 2a	pbl Assay Science	Cat#11100-1
D-Luciferin ethyl ester	Biomol	Cat#ABD-12515
Doxycycline	Sigma Aldrich	Cat# D5207
NativePAGE Novex 4%–16% Bis-Tris gels	Thermo Fisher	Cat#BN1002BOX
Nu-PAGE™ 4%–12% Bis-Tris protein gel	Thermo Fisher	Cat#NP0321BOX
ProLong Diamond Antifade Mountant	ThermoFisher	Cat# P36961
PEI	Polysciences	Cat#24765
Cyclohexamide	Serva	Cat#10700.02
Digitonin	Carl Roth	Cat#HN76.1
Propidium iodide	SigmaAldrich	Cat#P4170
NucLight Rapid Cell Dye	Sartorius	Cat#4717
Protein G Sepharose 4 FastFlow beads	GE Healthcare	Cat# 17061801
cOmplete protease inhibitor, EDTA free	Roche	Cat# 04693132001
NEM	Thermo Fisher	Cat#23030
Lithium Sample Buffer	Thermo Fisher	Cat#84788
Poly I:C	Invivogen	Cat# tlrl-pic
SARS-CoV-2 RNA	Twist Bioscience	Cat#102024
Critical commercial assays		
HiScribeTM T7 Quick HighYield RNA Synthesis Kit	New England Biolabs GmbH	Cat#E2050S
Click-iT® Plus OPP Protein Synthesis Assay	Thermo Fisher Scientific	Cat#C10456
TWIST Exome 2.0 kit	twistbioscience	N/A
QIAamp DNA Blood Mini kit	Qiagen	Cat# 51104
ReliaPrep™ RNA Miniprep Systems	Promega	Cat#Z6010
NucleoSpin RNA Plus isolation kit	Macherey Nagel	Cat#740984.25
PrimerScript RT (gDNA Eraser)	Takara	Cat#RR047B
PowerUp™ SYBR™ Green Master Mix	Applied Biosystems Thermofisher	Car#A25776
SuperSignal West Femto kit	Thermo Fisher Scientific	Cat#34096
QIAamp Viral RNA Kits	Qiagen	Cat#52904
TaqMan Fast Virus 1-step master mix	Thermo Fisher	Cat#4444436
TaqMan™ Microbe Assay Type 3, Small	Thermo Fisher	Cat#A41333
OAS1 primer probe Hs00973635_m1	Thermo Fisher	Cat#4331182
IFNB1 primer probe Hs01077958_s1	Thermo Fisher	Cat#4331182
TBP primer probe Hs00427620_m1	Thermo Fisher	Cat# 4331182

(*Continued on next page*)

Please cite this article in press as: Merold et al., Structural basis for OAS2 regulation and its antiviral function, Molecular Cell (2025), https://doi.org/10.1016/j.molcel.2025.05.001

Continued

REAGENT or RESOURCE	SOURCE	IDENTIFIER
Deposited data		
Human OAS2	This paper	PDB: 9H1Z
Human OAS2 map	This paper	EMDB: EMD-51786
RNA-seq	This paper	ArrayExpress: E-MTAB-14791
Human OAS2-RNA MD Simulation	This paper	https://doi.org/10.5281/zenodo.14753364
Unprocessed WB and microscopy data	This paper	https://doi.org/10.17632/tvgpf9t2jm.1
RNA-seq dataset THP-1 cells with *OAS2* MIS-C mutations	Lee et al.[34]	NCBI-SRA: PRJNA898284
Experimental models: Cell lines		
HEK293T	ATCC	Cat#CRL-11268
HEK293T *RNASEL* KO monoclonal cells	This paper	N/A
HEK293T NTC KO monoclonal cells	This paper	N/A
A549	Georg Kochs	N/A
Primary BJ HFF	Andreas Pichlmair lab, Huang et al.[91]	N/A
A549 *OAS2* KO	This paper	N/A
A549 NTC KO	This paper	N/A
A549 *OAS2* KO OAS2 WT KI cells	This paper	N/A
A549 *OAS2* KO OAS2 C652S KI cells	This paper	N/A
A549 *OAS2* KO OAS2 G2A KI cells	This paper	N/A
A549 *OAS2* KO OAS2 G2A C652S KI cells	This paper	N/A
A549 *OAS2* KO OAS2 F524L KI cells	This paper	N/A
HeLa H1	ATCC	Cat# CRL-1958
BJ HFF hTert$^+$	Andreas Pichlmair, Huang et al.[91]	N/A
Vero E6/TMPRSS2	Dr. Makoto Takeda, National Institute for Biological Standards and Control (NIBSC)	Cat#100978
Experimental models: Organisms/strains		
Trichoplusia ni cells	Expression Systems	N/A
Spodoptera frugiperda sf9 cells	Expression Systems	N/A
Oligonucleotides		
See Table S2		N/A
Recombinant DNA		
OAS plasmid constructs see Table S2	This paper	N/A
pET-28M-SUMO1-human OAS1 p46	This paper	N/A
pET-28M-SUMO1-human OAS1 p42	This paper	N/A
pACEBac1_N-6xHis_3C_hOAS3 p100	This paper	N/A
2′5′-OA biosensor RNase L-Luciferase plasmid	Alexei Korennykh, Chitrakar et al.[62]	N/A
pACEBac1_N-6xHis_3C_hOAS2 p71	This paper	N/A
pACEBac1_N-6xHis_3C_hOAS2 p69	This paper	N/A
pACEBac1_N-6xHis_3C_hOAS2-C652S	This paper	N/A
pACEBac1_N-6xHis_3C_hOAS2-p71 FL D153A S150A	This paper	N/A
pLentiCRISPRv2 (hygromycin)	Stringer et al. (2019)[92]	Addgene plasmid # 98291
pLIX403 (puromycin)	David Root	Addgene plasmid #41395
pLenti CMV/TO Zeo_GW (zeocin)	Campeau et al. (2009)[93]	Addgene plasmid # 17294
pMD2-VSVG	Andreas Pichlmair[89]	N/A
pCMV-Gag-Pol	Andreas Pichlmair[89]	N/A
pCG_ACE2_IRES_eGFP	Xie et al. (2023)[94]	N/A
pCR XL TOPO OC43 N fragment	This paper	N/A
pCR XL TOPO NL63 N fragment	This paper	N/A

(*Continued on next page*)

Please cite this article in press as: Merold et al., Structural basis for OAS2 regulation and its antiviral function, Molecular Cell (2025), https://doi.org/10.1016/j.molcel.2025.05.001

Continued

REAGENT or RESOURCE	SOURCE	IDENTIFIER
pCG Nef (STOP) IRES eGFP (vector control)	Greenberg et al.[95]	N/A
pCG Nef (STOP) IRES BFP (vector control)	Greenberg et al.[95]	N/A
EGFP-GalT	Cole et al.[72]	Addgene plasmid #11929
Software and algorithms		
ChimeraX 1.8	Pettersen et al.[96]	https://www.rbvi.ucsf.edu/chimerax/
CryoSparc 4.5.3	Punjani et al.[97]	https://cryosparc.com/
Alphafold3	Abramson et al.[59]	https://alphafoldserver.com
Coot 0.9.8.91	Emsley and Cowtan[98]	https://www2.mrc-lmb.cam.ac.uk/Personal/pemsley/coot/
Phenix 1.20.1-4487	Adams et al.[99]	https://www.phenix-online.org/
Prism 10	GraphPad Software	https://www.graphpad.com
Topaz	Bepler et al.[100]	https://emgweb.nysbc.org/topaz.html
Weblogo3	Crooks et al.[101]	https://weblogo.threeplusone.com
MAFFT7	Katoh et al.[102]	https://mafft.cbrc.jp/alignment/server/
Jalview 2.11.4.1	Waterhouse et al.[103]	https://www.jalview.org
GROMACS 2023.1	Abraham et al.[104]	https://www.gromacs.org/
GROMACS 2023.4	Abraham et al.[104]	https://www.gromacs.org/
PyMOL 3.0.3	Schrödinger, LLC	https://www.pymol.org
AmberTools 21	Case et al.[105]	https://ambermd.org/
APBS	Jurrus et al.[106]	https://www.poissonboltzmann.org/
MDAnalysis	Michaud-Agrawal et al.[107,108]	https://www.mdanalysis.org/
fd_helix.c	Case et al.[105]	https://casegroup.rutgers.edu/fd_helix.c
Contact Map Explorer	Swenson and Roet[109]	https://contact-map.readthedocs.io/
Fiji (ImageJ 2.9.0)	Schindelin et al.[110]	https://imagej.net/software/fiji/
Huygens Professional 19.10	Scientific Volume Imaging	https://svi.nl/Download
Incucyte S5 software	Sartorius	N/A
salmon 1.10.3	Patro et al.[111]	N/A
tximport 1.30.0	Soneson et al.[112]	https://bioconductor.org/packages/release/bioc/html/tximport.html
DESeq2 1.42.1	Love et al.[113]	https://bioconductor.org/packages/release/bioc/html/DESeq2.html
limma 3.58.1	Ritchie et al.[114]	https://bioconductor.org/packages/release/bioc/html/limma.html
ggplot2 3.4.4	Wickham[115]	https://cran.r-project.org/web/packages/ggplot2/index.html
MaxQuant 2.0.4.0	Cox & Mann[116], Tyanova et al.[117]	https://maxquant.org
Skyline 24.1	MacLean et al.[118]	https://skyline.ms/project/home/software/Skyline/begin.view
varvis genomics platform	Varvis	https://www.varvis.com/index.html
RStudio 2024.09.1+394	Posit	https://posit.co/download/rstudio-desktop/
SnapGene	SnapGene	https://www.snapgene.com

EXPERIMENTAL MODEL AND STUDY PARTICIPANT DETAILS

Escherichia coli strains

E. coli DH5alpha was used for cloning. *E. coli STBL3* was used for cloning for plasmids used for lentivirus generation. *E. coli* Rosetta was used for recombinant protein expression. *E. coli* DH10alphaMultiBac was used for cloning of expression constructs for baculovirus generation and insect cell expression.

Molecular Cell
Article

CellPress
OPEN ACCESS

Virus strains

IAV SC35M PB2 2A GFP was kindly provided by Martin Schwemmle, YFV YF-17D and YFV YF-17D-Venus were kindly provided by Simon Rothenfußer, RVFV-GFP, LACV (rec wt) and BUNV wt were kindly provided by Friedemann Weber, VACV-V300-GFP was kindly provided by Joachim Bugert, HSV1(17+)Lox-GFP) was kindly provided by Beate Sodeik, VSV-GFP-Indiana, EMCV, THOV-ML$^-$, ZIKV H/PF/2013 and EMCV were from Andreas Pichlmair.

Human rhino virus 16 (HRV16) was purchased from ATCC, cat# VR-283. For HCoV-OC43 (ATCC cat# CR-1558TM) and NL63 (kindly provided by Lia van der Hoek) propagation, Huh-7 or LLC-MK2 cells were inoculated with a MOI of 0.1 in Dulbecco modified Eagle medium supplemented with 2% FCS. Cells were incubated at 33°C. SARS-CoV-2 (strain Netherlands/01/NL/2020, European Virus Archive, cat# 010V 03903) was propagated on Vero E6 infected at an MOI of 0.003 in serum-free medium.

Insect cell lines

Spodoptera frugiperda Sf9 insect cells were used for baculovirus propagation. *Trichoplusia ni* High five cells were used for baculovirus infection for protein expression. Insect cell lines were maintained in Insect Cell Culture Medium (Protein Free, ESF 921) supplemented with antibiotics (penicillin, streptomycin) at 27°C, 130 rpm. Cells were passaged twice a week to a density 0.75–1*10^6 cells/ml for Sf9 cells and 0.5*10^6 cells/ml for High Five cells.

Mammalian cell lines and primary cells

HEK293T, A549, Hela H1 and BJ hTERT$^+$ HFF cell lines and BJ primary HFF cells were cultured in DMEM supplemented with 10% FBS at 37°C in 5% CO_2. Vero E6/TMPRSS2 cells were cultured in DMEM supplemented with 10% FBS, 2mM L-glutamine, 100 units/ml penicillin, 100 μg/ml streptomycin at 37°C in 5% CO_2. HEK293T, A549 and Hela H1 cells were passaged at a dilution 1:10 by washing with PBS and detached with 0.25% trypsin. BJ fibroblasts were passaged at a dilution 1:5 by washing with PBS and detached with 0.25% trypsin. Fibroblasts from OAS2 patient and healthy controls (three female donors: WT1 age 10 years 7 months, WT2 age 11 years, WT3 age 5 years 1 month) were derived from skin biopsies. Passage-matched primary human fibroblasts (passages 4 to 20) were cultured in Dulbecco's modified Eagle's medium (DMEM, Sigma, D5671) supplemented with 2 mM L-glutamine, 1x antibiotics/antimycotics, 1x non-essential amino acids (NEAA), and 10% fetal bovine serum (FBS) at 37 °C and 5% CO_2. All cell lines were regularly tested negative for mycoplasma contamination using TaKaRA PCR Mycoplasma Detection Set (TaKaRa).

METHOD DETAILS

Protein expression and purification

Human OAS2 wild-type and OAS2 constructs were cloned into a modified pACBac1 vector with N-terminal His-tag. The plasmid was transformed into *E. coli* DH10alphaMultiBac and plated on LB-agar plates containing 7 μg/ml gentamicin, 50 μg/ml kanamycin, 12.5 μg/ml tetracyline, 0.05 mM isopropyl thiogalactoside (IPTG), and 0.1 mg / ml X-Gal. Baculovirus DNA was extracted using NucleoBond Xtra Midi Kit (Macherey-Nagel) and transfected in *Spodoptera frugiperda* Sf9 insect cells. The Baculovirus was propagated twice in Sf9 cells and used for 1:100 infection of 2 L *Trichoplusia ni* High five cells at a concentration of 1.0 x 10^6 cells/mL. Cells were cultured for 72 h at 27°C and harvested by centrifugation.

Cells were lysed by sonification in lysis buffer (20 mM HEPES pH 7.5, 400 mM NaCl, 10% glycerol, 30 mM imidazole, 1 mM β-mercaptoethanol, protease inhibitor (100 mM PMSF, 200 mM benzamidine, 200 μM pepstatin A, 60 μM leupeptin). To clear the lysate, sample was centrifuged at 20.000 rpm for 1h at 4°C. Cleared lysate was added to equilibrated Ni-NTA resin (Macherey-Nagel) and incubated for 2h at 4°C. The beads were washed with 1 CV with lysis buffer, 3 CV with wash buffer (20 mM HEPES pH 7.5, 1 M NaCl, 10% glycerol, 30 mM imidazole, 1 mM β-mercaptoethanol, protease inhibitor) in batch. The last washing step of 1 CV lysis buffer was performed on gravity flow column. The protein was eluted in 10 mL fractions with elution buffer (20 mM HEPES pH 7.0, 200 mM NaCl, 10% glycerol, 300 mM imidazole,1 mM β-mercaptoethanol, protease inhibitor). The elution was diluted 1:3 in buffer A (25 mM HEPES pH 7.0, 100 mM NaCl, 2 mM DTT) and applied to a 5 mL HiTrap heparin HP column (Cytiva). The bound protein was eluted with 5 CV buffer B (25 mM HEPES pH 7.0, 1 M NaCl, 2 mM DTT). Fractions were pooled and loaded on a S200 Superdex 10/300 GL (Cytiva) in SEC buffer (20 mM HEPES, pH 7.0, 250 mL NaCl, 1 mM TCEP). Purified proteins were concentrated to 2 mg/mL, flash frozen in liquid nitrogen and stored at -80°C. N-terminally His-tagged human OAS3 was cloned in pACEBac1. Purification was performed as described above, but frozen in final concentration of 3 mg/mL. Human OAS1 was purified as described before.[119] Briefly, His-OAS1 in pET-SUMO was expressed in *E. coli* Rosetta cells, induced with 0.4 mM IPTG and grown overnight at 18°C. Cells were lysed by sonification in lysis buffer (20 mM HEPES pH 7.5, 400 mM NaCl, 10% glycerol, 30 mM imidazole, 1 mM β-mercaptoethanol, protease inhibitor (100 mM PMSF, 200 mM benzamidine, 200 μM pepstatin A, 60 μM leupeptin). Cleared lysate was loaded on Ni-NTA resin (Macherey-Nagel) in gravity flow column and washed 1 CV with lysis buffer, 3 CV with wash buffer (20 mM HEPES pH 7.5, 1 M NaCl, 10% glycerol, 30 mM imidazole, 1 mM β-mercaptoethanol, protease inhibitor) and 1 CV lysis buffer. The protein was eluted in 10 mL fractions with elution buffer (20 mM HEPES pH 7.5, 200 mM NaCl, 10% glycerol, 300 mM imidazole,1 mM β-mercaptoethanol, protease inhibitor) and dialyzed overnight against dialysis buffer (25 mM HEPES pH 7.5, 100 mM NaCl, 2 mM β-mercaptoethanol). During dialysis, His-OAS1 was cleaved with SUMO protease 1 (in-house production). The sample was loaded on a 5 mL HiTrap heparin HP column (Cytiva) with buffer A (25 mM HEPES pH 7.5, 100 mM NaCl, 2 mM DTT) and eluted with 5 CV

Please cite this article in press as: Merold et al., Structural basis for OAS2 regulation and its antiviral function, Molecular Cell (2025), https://doi.org/10.1016/j.molcel.2025.05.001

buffer B (25 mM HEPES pH 7.5, 1 M NaCl, 2 mM DTT). Fractions were pooled and loaded on a HiLoad 16/600 Superdex 75 size exclusion chromatography column (Cytiva) in 20 mM HEPES pH 7.5, 250 mM NaCl, 1 mM TCEP. Purified OAS1 was pooled and stored at -80°C.

Cryo-electron microscopy grid preparation

For cryo-em experiments, OAS2 wild type protein was diluted to 5 μM in 25 mM HEPES pH 7.5, 85 mM NaCl and 1 mM TCEP and octyl-β-glucoside was added to final concentration of 0.05%. Quantifoil Cu 200 R2/1 grids were plasma glow discharged for 7s at 20 mA (GloQube, Quorum). Grids were prepared with a Leica EM GP plunge freezer (Leica), at 10 °C and 90% humidity. 4.5 μL protein sample was applied to grids and blotted 2.0 s before vitrification in liquid ethane.

Cryo-electron microscopy data acquisition

Data were collected on a Titan Krios G3 transmission electron microscope (Thermo Fisher Scientific) used at 300 kV and a Gatan K2 Summit direct electron detector operated in counting mode and an energy filter. Data acquisition was automated with EPU software package (Thermo Fisher Scientific). 5708 movies were collected with defocus values ranging from -1.4 and -2.9 μM, pixel size of 1.059 Å and total electron dose of 50 $e^{-}Å^{-2}$. A representative micrograph is shown in SI. Figure 1B.

Cryo-electron microscopy data processing

Micrograph movies were motion corrected and dose-weighted using MotionCor2.[120] The CTF parameters of the datasets were estimated with CTFFIND4.[121] All cryo-em data processing steps were performed using cryoSPARC 4.5.3. The exact processing scheme, data collection and refinement statistics are depicted in Figure S1C; Table 1. 499 particles were manually picked on 5708 micrographs, extracted using 180 px box size and sorted by 2D classes. Topaz train was used for further, refined particle picking. The resulting 1729799 particles were used to generate an 3D ab-initio reconstruction and subjected to heterogeneous refinement. The best classes were selected for local CTF refinement and homogeneous refinement. The selected particles were then 3D classified. The best 3D classes were used for final homogeneous, non-uniform refinement and local refinement to obtain a map with a final resolution of 3.30 Å, calculated with the gold-standard Fourier shell correlation criterion (FSC = 0.143).

Model building and Figure preparation

Predicted structure of OAS2 from Alphafold1 (AF-P29728-F1) was rigid-body fitted to the electron density in UCSF ChimeraX.[122] Model building and iterative refinement were performed in Coot 0.9.8.6 with secondary structure restrains and Phenix 1.20. Figures were prepared using UCSF ChimeraX.[96]

In-vitro OAS activity assay

The activity of OAS was monitored by indirect colorimetric assay, measuring the byproduct pyrophosphate of the oligoadenylate synthesis.[119] OAS protein was incubated with dsRNA (concentrations indicated for each experiment) in reaction buffer (25 mM HEPES pH 7.0, 7 mM $MgCl_2$, 10 mM NaCl, 1 mM TCEP, 2 mM ATP) in a total reaction volume of 150 μL at 37°C for 120 min. For dose response analysis of OAS proteins, 100 nM protein were incubated with 5–500 nM 82 bp dsRNA for 20 min at 37°C. To quench the reaction, 10 μL aliquots were added to 2.5 μL 0.25 M EDTA, pH 8.0 in 96 well plate at 0, 5, 10, 20, 40, 60, 80, 100 and 120 min. 10 μL 2.5 % (w/v) ammonium molybdate in 2.5 M H_2SO_4 and 10 μL 0.5 M β-mercaptoethanol was added to each well and the final volume were adjusted to 100 μL. The produced molybdophosphoric acid was reduced to molybdenum blue complex that was measured at absorbance at 580 nm. Data were compared with pyrophosphate standard and analyzed using non-linear regression in GraphPad Prism 8.

EMSA (electrophoretic mobility shift assay)

The affinity of OAS proteins to dsRNA was determined by electromobility shift assays (EMSA). RNA (200 nM) was titrated to increasing concentrations of OAS protein (0–14 μM) in binding buffer (5 mM $MgCl_2$, 25 mM HEPES pH 7.0, 10 mM NaCl, 1 mM TCEP). The reaction was incubated for 10 min at RT and mixed with glycerol to an end concentration of 10%. Native TB gels (8%) were pre-run for 30 min. Samples were loaded and electrophoresis was performed at 4°C for 50 min at 200 V in 0.5x TB running buffer. Gels were stained in GelRed (Biotium) for 30 min at RT.

In-vitro Transcription

3p-dsRNA-hp was synthesized by *in vitro* transcription (IVT) from a dsDNA template (Metabion, Munich) using the HiScribe™ T7 Quick HighYield RNA Synthesis Kit (New England Biolabs GmbH, Frankfurt, Germany) according to the manufacturer's protocol for small RNAs. DNase I (New England Biolabs GmbH, Frankfurt, Germany) was added to the IVT reaction to remove the template DNA for 30 min at 37°C. A two-step purification protocol was used to achieve high purity RNA transcripts. First, RNA transcripts were separated from residual enzymes by phenol-chloroform extraction followed by ethanol precipitation. Second, the product was further separated from IVT by-products using a 12% TBE-urea polyacrylamide gel electrophoresis (PAGE). The RNA was visualized via UV shadowing on a silica-coated TLC plate, excised and crushed into small gel pieces by centrifuging it at maximum speed through

Please cite this article in press as: Merold et al., Structural basis for OAS2 regulation and its antiviral function, Molecular Cell (2025), https://doi.org/10.1016/j.molcel.2025.05.001

CellPress
OPEN ACCESS

a perforated 0.5 ml tube into a 1.5 ml collection tube. 3p-RNA-hp was eluted from the gel with 0.5 M ammonium acetate by shaking overnight at 16°C, precipitated with ethanol (3 volumes) and dissolved in nuclease-free water. Products were quality controlled by mass spectrometry (ESI-TOF) at Metabion, Munich.

Mass photometry

Mass photometry measurements of OAS proteins were performed with Two MP mass photometer (Refeyn). Samples were diluted to 50 nM in filtered buffer (25 mM HEPES pH 7.0, 50 mM NaCl, 1 mM TCEP) and movies were recorded for 60s. Data were analyzed using AquireMP software (Refeyn).

MD simulations

We used all-atom MD simulations to characterize the conformational dynamics and to predict the RNA-binding site on OAS2. OAS2 was simulated as monomer and dimer. Both systems were simulated with and without dsRNA with 44 bp. All systems were prepared with a bulk salt concentration of 100 mM NaCl. The force fields parameters were taken from the AMBER ff19SB force field,[123] RNA force-field parameters from the AMBER99sb*ILDN-parmbsc0- χ-OL3 force field, OPC water[124] and ion force fields from.[125,126] After equilibration, the production runs were done in the NPT ensemble with velocity-rescaling thermostat[127] with a time constant of 1 ps^{-1} and Parinello-Rahman barostat[128] with a coupling constant of 5.0 ps were used. The OAS2 monomer and dimer were simulated for 100 ns each at physiological conditions. Configuration sampling simulations of the dsRNA-OAS2 complexes at 400 K were followed by contact analysis and consecutive simulations at physiological temperature and pressure. More than 2.8 μs were used to identify key residues involved in RNA binding.

In addition, the protonation state of the zinc binding site was carefully adjusted to correctly account for the zinc binding which is known to play a crucial role for the stability of the OAS2-Zn^{2+} complex.

Simulation setup

Using AmberTools21[105] the protein topology and force field files were created based on the OAS2 cryo-em structure using the latest AMBER protein force field ff19SB.[123] The AMBER99sb*ILDN-parmbsc0- χ-OL3 force field was used for RNA, which builds on the AMBER99 force field[129] and includes additional corrections to the nucleic acid backbone behavior[130] and glycosidic torsion.[131]

The unstructured, extended terminal regions of the protein were removed from the cryo-em, structure, to reduce the computational costs since they are unlikely to affects dsRNA binding. Initial simulations confirmed the integrity and stability of the cryo-em structure. For MD simulations of the OAS2 monomer, half of the experimental dimer structure was used as starting point. All simulations employed the OPC water model.[124] Na^+ and Cl^- parameters were originally parameterized for TIP3P[125] but were used in combination with OPC water after ensuring that solvation free energies and activity derivatives were in close agreement with experiments. For the centrally coordinated Zn^{2+} ion specifically for OPC optimized parameters were used.[126]

The protonation states of the cysteine and histidine residues, which form the zinc coordination site essential for OAS2 dimer stability, were modified to maintain stable coordination with the Zn^{2+} ion. Preliminary simulations indicated that the standard protonation states at physiological pH result in the dissociation of the zinc cation from the coordination site. This unphysiological behavior is likely caused by changes of the protonation state in the presence of a metal ion in the binding site. Such changes are neglected by the standard Amber tools. To provide a more realistic description of the metal binding site, the sulfur atoms of the cysteine residues were deprotonated and for the histidine residues the protonation site was shifted from the ε to the δ position.

The 44 bp dsRNA (sequence: GCGCUAUCCAGCUUACGUAGAGUAGCAUCGUACGAUGCUACGGC) for the simulations of the complex was generated using the *fd_helix.c* function (David A. Case 2018, https://casegroup.rutgers.edu/fd_helix.c). Using PyMOL [The PyMOL Molecular Graphics System, Version 3.0.3 Schrödinger, LLC.], the dsRNA structure was aligned to the 18 bp piece of dsRNA bound to the crystal structure of OAS1-dsRNA complex.[37,38] The initial structures were solvated, neutralized and further Na^+ and Cl^- ions were added to achieve a bulk concentration of 0.1 mol/l. After that the energy was minimized using the Steepest Decent and conjugate Gradient algorithms until machine precision was reached.

All simulations were done with GROMACS 2023.1 and 2023.4.[104] Coulombic interactions were handled using the Particle Mesh Ewald (PME) method with PME order of 4 and a Fourier spacing of 0.16. Close Coulomb real space interactions were cut off at 1.2 nm and Lennard-Jones (LJ) interactions were cut off after 1.2 nm without potential shift. Long-range dispersion corrections for energy and pressure were applied to account for errors stemming from truncated LJ interactions. Periodic boundary conditions were used. The Verlet neighbor-searching list with cut off 1.2 nm was used and updated every 10 steps. The leap-frog algorithm was used to integrate Newton's equations of motion. A time step of 2 fs was used as hydrogen bonds were constrained using the Lincs algorithm.[132]

A total of four different systems were modelled and simulated: The OAS2 monomer and dimer were simulated to investigate their conformational dynamics and judge their stability. They were simulated in cubic boxes of lengths 10.6 nm (monomer) and 11.4 nm (dimer). They contained approximately 146000 (monomer) and 192000 atoms (dimer). To locate the RNA binding site on OAS2 and asses the dynamics of the RNA-protein complex, a 44bp dsRNA was simulated together with the OAS2 monomer and dimer. These systems were set up in dodecahedral boxes with the dimensions (14.1 x 14.1 x 9.9) nm^3 (monomer) and (16.5 x 16.5 x 11.7) nm^3 (dimer) and contained around 260000 (monomer) and 421000 atoms (dimer).

OAS2 monomer and dimer simulations

After minimization, the systems were equilibrated in the NVT ensemble for 4 ns at the physiological temperature of 310.15 K. All NVT equilibration simulations were done using the Berendsen thermostat[133] with a coupling constant of 0.1 ps. This was followed by 4 ns NPT equilibration, which employed the velocity rescaling algorithm[127] with a coupling constant of 0.1 ps and the Berendsen barostat using isotropic pressure coupling, a coupling constant of 2.0 ps, reference pressure of 1 bar and a compressibility of 4.5 $*10^{-5}$ bar^{-1}. Position restraints (1000 kJ/mol*nm^2) were put on heavy protein atoms during NVT and NPT equilibration. After pre-equilibration the systems containing OAS2 monomer and dimer were simulated without restraints for 100 ns each in NPT ensemble, using the velocity rescaling thermostat with a coupling constant of 1.0 ps and the Parinello-Rahman barostat[128] with a coupling constant of 5.0 ps, reference pressure of 1 bar and a compressibility of 4.5 $*10^{-5}$ bar^{-1}.

dsRNA binding site prediction simulations

For the predictions of the dsRNA binding site, the systems were simulated at a higher temperature to speed up the conformational sampling and to overcome possible energy barriers associated with binding and unbinding of the RNA. An initial temperature of 400 K was used. Once the RNA was bound, the systems were cooled to physiological temperature (see below).

For the OAS2 monomer and dimer, 10 simulation runs of 100 ns were initiated from the same equilibrated structures. The simulations were performed in the NVT ensemble at 400K using the velocity rescaling thermostat with a coupling constant of 0.1 ps. The starting velocities for each run were drawn randomly from Maxwell-Boltzmann. To prevent the RNA from unzipping at elevated temperatures, restraints were applied to the distances between the two terminal nucleobases at each end. Also, the position of the zinc ion within the binding site was restrained.

Potential binding structures were identified by analysing the number of close contacts between dsRNA and protein. For the dimer and monomer systems respectively, four potentially binding conformations were identified showing the maximum numbers of close contacts formed between domain I of the OAS2 monomer or dimer and the dsRNA. These structures were then taken as the starting points for additional equilibration at 310.15 K in NVT and NPT ensemble as described above. The pre-equilibrated dsRNA-OAS2 complexes were successively used for 100 ns production runs in NPT ensemble. The prediction of the key residues involved in the binding of dsRNA was based on these productions runs.

Number of close contacts

The number of close contacts between dsRNA and OAS2 was calculated using GROMACS and the Contact Map Explorer [David W. H. Swenson and Sander Roet, https://github.com/dwhswenson/contact_map] Python package which builds on the MDTraj package.[134] Close contacts were defined as instances where the distance between protein and RNA atoms was less than 0.35 nm. In line with the experimental findings of a minimal RNA length requirement for OAS2 activation, the analysis of close contacts was focused on domain I of OAS2.

Contact frequencies

Contact Frequencies were calculated using the Contact Map Explorer [David W.H. Swenson and Sander Roet, https://github.com/dwhswenson/contact_map] Python package which builds on the MDTraj package[134] and additional python code. Close contacts were defined as protein and RNA atoms being closer than 0.35 nm. The frequencies were normalized in a way that a close contact of a protein residue with a dsRNA atom over the length of one whole 100 ns simulation resulted in a contact frequency of 1. Values above 1 either correspond to close contacts between a certain protein residue and multiple RNA atoms or one close contact that occurred for a length exceeding that of a single 100 ns simulation.

The electrostatic surface potential was calculated using the ChimeraX. The structure shown is based on one representative binding conformation extracted from one of the production runs. The structure shows the averaged backbone coordinates over a simulation time of 100 ns. The RMSD values were calculated as detailed below.

RMSD

RMSD values were calculated using the Python library MDAnalysis[107,108] by aligning each frame of a 100 ns trajectory to the cryo-em structure and calculating the RMSD. For alignment and RMSD calculation only backbone atoms were considered. Figures showing the RMSD values by color were created using ChimeraX. They show structures averaged over 100 ns of simulation time. The corresponding RMSD values are based on alignments of the averaged structures obtained from MD simulations to the cryo-em structure. For the OAS2 monomer, half of the cryo-em dimer structure was used as a reference.

Generation of cell lines

Two different gRNA sequences for *OAS2* and non-targeting control (NTC) knockout were cloned in pLentiCRISPRv2 vector (Addgene) with hygromycin resistance. OAS2 guide RNA (gRNA) sequences were designed using the Synthego (https://design.synthego.com) design tool. Non-targeting control sequences were obtained from the GeCKO v2.0 library.[135] Primers encoding target guide RNA sequences were annealed and used for ligation with linearized vector from restriction digest with BsmbI enzyme. Primer sequences containing overhangs for ligation are listed in the Table S2. Successful cloning was verified by sequencing and target vectors were further used for lentivirus generation.

Please cite this article in press as: Merold et al., Structural basis for OAS2 regulation and its antiviral function, Molecular Cell (2025), https://doi.org/10.1016/j.molcel.2025.05.001

CellPress
OPEN ACCESS

For generation of doxycycline-inducible OAS2 KI cell lines, OAS2 p71 N- and C-terminal fragments were amplified from respective OAS2 WT, OAS2 G2A, OAS2 C652S or OAS2 F524L constructs in pCDNA4 vector using primers listed in the Table S2. Two fragments from N-terminus and C-terminus were amplified from OAS2 gene to introduce silent mutations and mismatches in gRNA binding site and introduce overlaps with target vector pLIX-403 for Gibson assembly ligation. Target vector pLIX-403 was linearized using NheI and BamHI restriction enzymes. Inserts from OAS2 N- and C-termini to generate respective WT, G2A, C652S, G2A C652S or F524L constructs were used for Gibson assembly with linearized pLIX-403 vector and transformed into STBL3 *E.coli* strain.

For generation of *RNaseL* KO monoclonal HEK293T cell lines by transient transfection, two guide RNAs for *RNaseL* and NTC KO were first cloned into pLentiCRISPRv2 vector with hygromycin resistance as described above for *OAS2* gRNA cloning. *RNaseL* gRNA sequences were designed using CHOPCHOP web tool and are listed in the Table S2. Afterwards fragment encoding gRNA and Cas9 in pLentiCRISPRv2 vector and pLentiCMV/TO (zeocin resistance) vector were amplified by PCR to generate overlaps for Gibson assembly primers listed in the Table S2. Fragments were ligated using Gibson assembly and the resulting vector was used for cell line generation.

Lentiviral transductions were used to generate A549 *OAS2* KO cell lines reconstituted with doxycycline-inducible OAS2 constructs. For knockout generation lentiviral particles were generated by transfecting HEK293T cells with psPAX2 and pMD2.G-VSV-G packaging plasmids together with pLentiCRISPRv2 vector with hygromycin resistance encoding *S. pyogenes* CRISPR-Cas9 and two different gRNA sequences. Lentiviral particles were harvested 48h post transfection and used to infect A549 cells followed by selection with 500 μg/ml hygromycin one day post infection. Selection was terminated once there were no more viable control untransduced cells with hygromycin selection.

For reconstitution of OAS2 lentiviral particles were generated by transfecting HEK293T cells with psPAX2 and pMD2.G-VSV-G packaging plasmids together with transgene in pLIX_403 vector with puromycin resistance. Lentiviral particles were harvested 48h post transfection and used to infect A549 *OAS2* KO cells followed by selection with 1.5 μg/ml puromycin one day post infection. Selection was terminated once there were no more viable control untransduced cells with selection. *OAS2* KO and reconstitution was validated by WB analysis.

For monoclonal *RNaseL* KO cell line generation in HEK293T cells, cells were transfected with two different guides for *RNaseL* or NTC and *S. pyogenes* CRISPR-Cas9 in pLenti CMV/TO vector with zeocin resistance. 48h after transfection cells were selected with 400 μg/ml zeocin for 5–7 days until control transfected cells were not viable. Afterwards single cells were seeded into 96 well plate and grown for 7–10 days until formation of single colonies visible by bright-field microscopy. Single colonies were selected and expanded and KO was validated by WB analysis.

2′-5′ oligoadenylate (OA) biosensor analysis

Measurements of in vivo 2′-5′OA synthesis was performed as previously described by[62] using 2′-5′OA biosensor V6 (WT) and V6-Y312A variant lacking 2′-5′OA binding capacity. For the assay, 3x10^4 HEK293T cells were seeded into flat-bottom, white 96-well plates with two wells/ technical replicates per condition. The following day cells were transfected with 75ng V6 or V6-312A plasmid and 75ng OAS expression constructs using 0.4 μl Lipofectamine 2000 (Thermo Fisher Scientific). For OAS2 WT and F524L mixes in Figure 6 37.5ng of OAS2 plasmids in total and 75ng of V6 2′5′-OA biosensor were used. Forty-eight hours after transfection, cells were transfected with poly(rI:rC) dsRNA (1 and 3 μg/ml) using Lipofectamine 2000 and treated with 100 μM D-luciferin ethyl ester (BioMol). Luminescence was measured in 2h intervals over 8 hours and at 20–24h using Tecan plate reader. After the last measurement, cells were harvested and used for WB analysis to validate equal protein expression.

Western Blot analysis

For monitoring induction of OAS2 protein expression, cells were stimulated for 24h (unless stated differently in the figure legend) with 1 μg/ml doxycycline for A549 *OAS2* KO OAS2 KI cells lines or 500 or 1000U/ml IFN-α to induce endogenous OAS proteins in A549 or BJ primary and hTert$^+$ HFF cell lines. After stimulation cells were washed with PBS and harvested for Western blot analysis. Cells were lysed in NP-40 lysis buffer (50mM Tris-HCl pH 7.5, 150mM NaCl, 1% NP-40, 5mM EDTA) supplemented with 1X Complete protease inhibitor (Sigma-Aldrich) for 20–30min on ice. Soluble fraction was separated by centrifugation for 10min, 21'000xg, 4°C, mixed with 1x Laemmli Sample Buffer and boiled for 5–10min at 95°C. Protein was resolved by 10% SDS-PAGE and transferred to 0.45 μm PVDF membrane. Membranes were blocked in 5% non-fat dry milk, 0.1% Tween-20 in PBS and incubated with the following primary antibodies: anti-OAS2 (ProteinTech, 19279-1-AP), anti-OAS1 (Cell Signaling, 14498S), anti-OAS3 (ProteinTech, 21915-1-AP), anti-GAPDH (Santa Cruz, sc-47724), anti-FLAG-M2-HRP (Sigma Aldrich, A8592), anti-RNase L (Santa Cruz, sc-74405), anti OAS1 (ProteinTech, 14955-1-AP; in Hela H1 cells). Afterwards membranes were probed with species IgG-specific HRP-conjugated secondary antibodies goat anti-rabbit IgG (Dako, P0448) or horse anti-mouse IgG (Cell Signaling, 7076) or infrared Dye coupled secondary antibodies for Hela H1 cells. Immunoblots with HRP signal were developed with the SuperSignal West Femto kit (Thermo Fisher Scientific) and imaged with the Bio-Rad ChemiDoc Imaging System. Image Studio was used for capturing images with infrared Dye-coupled secondary antibodies.

For interferon-mediated OAS2 induction, wild-type (WT) and patient-derived (P) fibroblasts were stimulated with IFN-α (500 IU/ml) for 16 h or 24 h before cell lysis in RIPA buffer (50 mM Tris-HCl, pH 7.4, 150 mM NaCl, 1 mM EDTA, 1% Triton X-100, 1 mM Na3VO4

and 20 mM NaF) supplemented with 2 U/ml DNase I (Invitrogen), cOmplete protease inhibitor cocktail (Roche), and PhosSTOP (Roche). Hela H1 cells were lysed on ice with transmembrane lysis buffer (50 mM HEPES pH 7.4, 150 mM NaCl, 1% Triton X-100, 5 mM EDTA) supplemented with 1:500 protease inhibitor.

BN-PAGE analysis

BN-PAGE was performed using NativePAGE Novex 4%–16% Bis-Tris Gel System (Thermo Fisher Scientific) following manufacturer's instructions. 1.5x105 HEK293T cells were seeded per well in 24 well plates and the following day cells were transfected with 330ng plasmid DNA using 1ug PEI transfection reagent. 24–48h post transfection cells were harvested and lysed in 0.5% digitonin, 1x BN-PAGE sample buffer (50mM bisTris, 6N HCl, 50mM NaCl, 10% w/v glycerol, 0.001% Ponceau S, pH 7.2) supplemented with 1xcOmplete protease inhibitor (Sigma-Aldrich) on ice for 20–30min. Soluble fraction was separated by centrifugation for 30min, 21'000xg, 4°C. Before loading on the BN-PAGE gel lysates were supplemented with 0.125% Coomasie G-250. Purified recombinant protein for BN-PAGE was diluted in 25mM HEPES, pH 7.0, 1mM TCEP and mixed with 1x BN-PAGE sample buffer supplemented with 1xcOmplete protease inhibitor (Sigma-Aldrich) and mixed with 0.125% Coomasie G-250 before loading on the gel. Proteins were separated by running on ice at 150V for 60min in Anode buffer (50mM bisTris, 50mM Tricine, pH 6.8) in the outer chamber and in Dark cathode buffer (Anode buffer supplemented with 0.02% Coomasie G-250) in the inner chamber until the dye front reaches 1/3rd of the gel. Afterwards the gel was run at 250V for 60min in Light cathode buffer (Anode buffer supplemented with 0.002% Coomasie G-250) in the inner chamber until dye front reached the end of the gel. Protein was transferred to 0.45 μm PVDF membrane in 25mM Trizma base, 150mM glycine, pH 8.3, 20% methanol for 1h at 100V and fixed by incubation with 8% acetic acid for 15min at RT. Blocking and antibody incubations were performed as described in the Western blot analysis.

Immunofluorescence staining and imaging

For imaging of A549 cells, 3x10^4 cells were seeded in 8-well x-well cell culture chambers (Sarstedt) and following day cells were stimulated with 1 μg/ml doxycycline or 500U/ml IFN-α for 24h. For imaging of EMCV and YFV dsRNA and OAS2 in A549 cells, cells were stimulated with 1μg/ml doxycycline for 24h and infected with EMCV (MOI 0.15) or YFV (MOI 0.6) for 24h. BJ primary and hTert$^+$ fibroblasts were seeded at density 8000 cells per chamber and stimulated with 1000U/ml with IFN-α for 24h. HEK293T cells were seeded at the density 6x104 cells per chamber and transfected with 330ng plasmid DNA using PEI transfection reagent.

Cells were washed three times with PBS and fixed with 4% paraformaldehyde in PBS for 15–20min at RT followed by three washes with PBS. Cells were permeabilized with 0.1% Triton-X-1qq00 in PBS for 10min at RT, washed three times with PBS and blocked in 2% BSA in PBS, 0.1% Tween-20 for 30min at RT. Immunostaining was performed using primary antibodies: anti-OAS2 (R&D Systems, MAB1925-SP, 1:1qq00), anti-OAS2 (ProteinTech, 19279-1-AP,1:250), anti-GM130 (Thermo Fisher Scientific, 703794, 1:1qq00), anti-OAS1 (Cell Signaling, 14498S, 1:1qq00), anti-GM130 (ProteinTech, 66662-1-Ig, 1:500), anti-calnexin (R&D Systems, NB1qq00-1965SS, 1:200), anti-giantin (R&D Systems, NBP1-91937, 1:200), anti-TGN46 (R&D Systems, NBP1-49643SS), anti-Golgi 58K (1:200) and anti-dsRNA J2 (SCICONS, 1qq001qq0500). Antibody mixes were diluted in 2% BSA in PBS, 0.1% Tween-20 and incubated with cells for 1h at RT. Cells were washed three times with PBS and incubated with fluorophore-conjugated secondary antibodies: anti-rabbit AF488 (Cell Signaling, 4412S, 1:1qq000) and anti-mouse AF647 (Thermo Fisher Scientific, A31571, 1:1qq000) in 2% BSA in PBS, 0.1% Tween-20 together with DAPI (1:1qq000) for 1h at RT in the dark. Cells were washed three times with PBS and mounted using ProLong Gold antifade mountant (Thermo Fisher Scientific). Super-resolution Images were acquired using a Zeiss LSM 900 (Zeiss, Oberkochen, Germany) with an Airyscan 2 detector system using a Plan-APOCHROMAT 63×/1.4 Oil DIC Objective and 40×/1.2 Oil DIC Objective. Image processing and brightness adjustments were made using the ImageJ software version 1.54. Confocal images were acquired using an Olympus FV1qq0i microscope (Olympus, Tokyo, Japan) with a 60×/1.2 water immersion objective.

Primary OAS2 F524L and control fibroblasts were seeded on round 12 mm coverslips in 24-well plates at a density of 15,000 cells per well and incubated overnight. Cells were fixed with 4% formaldehyde for 20 min and permeabilized with 0.25% Triton X-1qq00 in PBS for 10 min at 21 °C. After blocking with 3% BSA/ 0.3% Triton X-100 in PBS for 1h at 4 °C, cells were incubated with the appropriate primary antibodies diluted in at 4 °C for 16h. Afterwards cells were incubated with corresponding Alexa Fluor-labeled secondary antibodies (Invitrogen, Alexa Fluor 488 goat anti-rabbit IgG, A11008; Alexa Fluor 594 goat anti-mouse IgG, A11032) diluted in 1% BSA/ 0.3% Triton X-100 containing PBS for 1 h in the dark at 21 °C. Cells were washed three times with PBS before mounting with Vectashield containing DAPI. Fluorescence images were captured using a LSM780 or a LSM980 confocal microscope (Zeiss).

For analysis of OAS2 localization at the Golgi membrane at either cytosolic or Golgi lumen, EGFP-GalT construct was used to establish and validate permeabilization protocol.[72] EGFP-GalT is a fusion construct between EGFP and Golgi protein GalT, which targets EGFP to the Golgi lumen. A549 cells were transfected with 330ng EGFP-GalT plasmid using 1ul PEI (1mg/ml). 48h later cells were washed with PBS and fixed with 4% paraformaldehyde for 15min at RT. Cells were permeabilized with either 0.1% Triton-X-100, which permeabilizes plasma and Golgi membranes or 5μM or 20μM digitonin, which permeabilizes plasma membrane but not Golgi membrane, for 10min at RT. Afterwards cells were washed three times with PBS for 5min and blocked in 2% BSA, PBS for 30–60min. Further immunostaining and imaging steps were performed as described above for A549 cells, except no Tween-20 was used for antibody solutions. For GFP staining anti-GFP antibody (Abcam) was used at a dilution 1:200. Successful permeabilization of plasma membrane only and not Golgi membrane by digitonin was verified by GFP fluorescence at the Golgi and lack of anti-GFP signal. Both GFP fluorescence and anti-GFP signal were observed with Triton-X-100 permeabilization. The same

permeabilization protocol was then applied to A549 cells stimulated with 500 U/ml of IFN-a for 24h to monitor localization of endogenous OAS2. Golgi marker GM130 was co-stained as a known Golgi marker facing cytosol.

Live cell imaging of viral replication

For virus screen stable A549 *OAS2* KO OAS2 WT KI cells were seeded at density 4000 cells/ well in 96 well plates in DMEM, 10% FBS and 1:2000 propidium iodide (1mg/ml stock) with two wells/ technical replicates per condition. The following day cells were stimulated with 1μg/ml doxycycline, 10U/ml IFN-α or a combination of both or media alone for control. 24h after stimulation cells were infected with a set of 11 viruses using two different MOIs for each virus: 1) GFP reporter viruses: IAV SC35M PB2 2A GFP (MOI 1, 0.1), YFV YF-17D-Venus (MOI 0.85, 0.1), RVFV-GFP (MOI 1, 0.1), VACV-V300-GFP (MOI 1, 0.1), HSV1(17+)Lox-GFP (MOI 1, 0.1) and VSV-GFP-Indiana (MOI 0.1, 0.01); 2) non-reporter viruses: LACV (rec wt) (MOI 1, 0.1), ZIKV (MOI 1, 0.1), BUNV wt (MOI 1, 0.1), THOV-ML$^-$ (MOI 1, 0.1) and EMCV (MOI 0.6, 0.06). Phase (cell confluence), red fluorescence intensity from propodium iodide and green fluorescence intensity for reporter viruses were measured every 3h over 72h post infection at 37°C, 5% CO2 using IncuCyte S5 fluorescence light microscopy screening platform (Sartorius). The virus replication for reporter viruses was quantified as integrated green fluorescence intensity per image normalized to cell confluence per image. Cell death was quantified as red fluorescence area per image normalized to cell confluence per image. Data were analysed using IncuCyte S5 Software (Sartorius).

For EMCV infection of stable A549 *OAS2* KO cells with OAS2 WT, OAS2 G2A, OAS2 C652S, OAS2 G2A C652S and OAS2 F524L KIs, cells were treated and analysed as described above.

Viral RNA detection

For analysis of intracellular EMCV RNA levels in A549 *OAS2* Ko Ki WT cells 4.5x10^4 cells/ well were seeded in 12 well plate. The following day cells were treated with 1 μg/ml doxycycline or 10U/ml IFN-α for 24h. Afterwards cells were infected with EMCV MOI 0.15 for 24h. Cells were then washed twice with PBS and cell pellets harvested for RNA isolation. For analysis of intracellular EMCV RNA levels in HEK293T cells 1.5x10^5 cells/ well were seeded in 24 well plate. The following day cells were transfected with 330ng target plasmid using 1 μl PEI (1mg/ml stock). Afterwards cells were infected with EMCV MOI 1 for 24h. Cells were then washed twice with PBS and cell pellets harvested for RNA isolation. For analysis of EMCV RNA levels total RNA was extracted using the NucleoSpin RNA Plus kit (Macherey-Nagel) according to the manufacturers' protocol. Total RNA was used for reverse transcription with PrimeScript RT reagent Kit with gDNA Eraser (TaKaRa) according to the manufacturers' instructions. Relative transcript quantification was obtained by qPCR with the transcript-specific primers (Table S2) and PowerUp SYBR Green master mix (Thermo Fisher) on a QuantStudio3 Real-time PCR system (Applied Biosystems). The oligonucleotides used for the analysis are listed in Table S2. Ct values were obtained using QuantStudio Design and Analysis software and averaged across technical replicates. The transcript levels were normalized to the levels of a housekeeping gene *GAPDH*.

For infection of HEK293T cells with coronaviruses HCoV-OC43, NL63 and SARS-CoV2 HEK293T cells were seeded at 3*10^5 cells/ml in 24-well plates and transfected with 50ng of hACE2 and 50ng of pCG plasmid expressing GFP (control) or OAS2 p69. After 24h cells were infected with 0.1 MOI of SARS-CoV-2, NL63 or OC43. NL63 and OC43 infected cells were incubated at 33°C and SARS-CoV-2 infected cells were incubated at 37°C. The following day cells were washed in PBS and fresh medium was added. Supernatants and cells were harvested 3 days post infection and centrifuged at 3000rpm for 3min to remove cell debris.

For analysis of OC43 RNA levels in supernatants, A549 cells were seeded at density 2x10^5 cells /ml into 12-well plates in DMEM, 10% FCS, 1μg/ml doxycycline in the presence or absence of 500U/ml of IFN-β. The following day cells were infected with OC43 at MOI 0.1 and incubated at 33°C. The following day cells were washed with PBS to remove input virus. Supernatants and cells were harvested 3 days post infection and used for measurement of viral copy numbers in the supernatants by RT-qPCR.

RNA from supernatant of seasonal coronaviruses-infected cells was isolated using QIAamp Viral RNA Kits (Qiagen) according to manufacturer's instructions. RT-qPCR was performed with TaqMan Fast Virus 1-step master mix (Thermo Fisher, catalog no. 4444436) and OneStepPlus real-time PCR system (96-well format). Custom primers and probes (5′ FAM-TAMRA 3′) were ordered from Biomers.net and are listed in the Table S2. Synthetic SARS-CoV-2 RNA (Twist Bioscience, catalog no. 102024) or linearized plasmids encoding OC43 or NL63 *N* gene fragments were used as a quantitative standard to obtain viral copy numbers. All reactions were run in triplicates.

Hela-H1 cells (passage 11) were transiently transfected using Lipofectamine 3000 (Thermo Fischer Scientific) with plasmid containing gene of interest or empty vector according to manufacturer's recommendations. 24 h post-transfection cells were infected with 0.1 MOI Human Rhino Virus 16 (HRV16) and cultured at 33 °C for 5 more days until cytopathic effects were observed. The supernatant from the infected cell cultures were collected 5 days post infection and the RNA was isolated using Viral RNA mini kit (Qiagen) according to manufacturer's instructions. RT-qPCR was performed using TaqMan Fast Virus 1-Step Master Mix and a OneStepPlus Real-Time PCR System (96-well format, fast mode). The primer-probes for microbe detection was used (Thermo Fisher Scientific).

RT-qPCR analysis

For analysis of *IFNB1*, *CXCL8*, *FOS* and *PTGS2* levels in A549 *OAS2* Ko Ki WT and OAS2 F524L cells 6250 cells/ well in 1ml DMEM, 10% FBS were seeded in 12 well plate. The following day cells were treated with 1 μg/ml doxycycline for 72h. Afterwards cells were infected with EMCV MOI 0.3 for 24h. Additionally, for *IFNB1* and EMCV *gp1* analysis cells were treated with doxycycline for 24h, 48h

Please cite this article in press as: Merold et al., Structural basis for OAS2 regulation and its antiviral function, Molecular Cell (2025), https://doi.org/10.1016/j.molcel.2025.05.001

and 72h and infected for 24h. Cells were then washed twice with PBS and cell pellets harvested for RNA isolation. Total RNA was extracted using the NucleoSpin RNA Plus kit (Macherey-Nagel) according to the manufacturers' protocol. Total RNA was used for reverse transcription with PrimeScript RT reagent Kit with gDNA Eraser (TaKaRa) according to the manufacturers' instructions. Relative transcript quantification was obtained by qPCR with the transcript-specific primers (Table S2) and PowerUp SYBR Green master mix (Thermo Fisher) on a qTower Iris PCR system (Analytik Jena). The oligonucleotides used for the analysis are listed in Table S2. Ct values were obtained using qTower Iris software and averaged across technical replicates. The transcript levels were normalized to the levels of a housekeeping gene GAPDH.

For RNA isolation and RT-qPCR analysis patient fibroblasts were seeded in a 24-well plate at a density of 150000 cells per well. The following day, after a media change, cells were treated overnight (~16 h) with 0.5 μg/mL poly(I:C) (LMW) / LyoVec (InvivoGen). RNA was then isolated from the cell lysates using RNeasy Plus Mini Kit (Qiagen) according to manufacturer's instructions. RT-qPCR for supernatants was performed using Luna Universal Probe One-Step RT-qPCR Kit. All primer-probes were purchased (Thermo Fischer).

RNA-seq and data processing

For RNA-seq sample preparation and RNA isolation was performed as described above for RT-qPCR with 72h of doxycycline stimulation followed by 24h of EMCV infection. Library preparation and sequencing was performed by Novogene using poly-A enrichment and 150bp paired-end sequencing using Illumina NovaSeq X Plus Series platform.

Fastq files with sequencing reads were mapped to hg38 human transcriptome with genome decoy using prebuilt index from refgenie with salmon[111](v1.10.3) using options—useVBOpt—seqBias. Transcript levels counts were imported using tximport[112] (v1.30.0) package and summarized to gene levels counts with EnsDb.Hsapiens.v86 package (DOI: 10.18129/B9.bioc.EnsDb.Hsapiens.v86) and used for differential expression analysis with DESeq2 (v1.42.1) package.[113] For differential expression analysis design formula "design = ~batch+Condition" to correct for batch effect. For plotting of PCA plots and heatmaps counts were transformed using variance stabilized transformation followed by removal of batch effect using limma (v3.58.1) package.[114,136] Differentially expressed genes were defined as $\log_2$ fold change $\leq$ -1 or $\geq$ +1 and adjusted p value $\leq$ 0.05. DEG analysis of RNA-seq are found in Table S1. Pathway analysis was performed using David analysis tool.[137]

For analysis of gene expression in THP-1 WT and *OAS2* KO RNA-seq samples and myeloid cells from MIS-C patient data were used from Lee et al. 2023.[34] THP-1 cell data for WT and *OAS2* KO were downloaded and analyzed as described above except without batch effect removal. For differential expression analysis 2h and 8h treatment time points were analyzed together as replicates for Lipofectamine + poly I:C condition versus Lipofectamine treatment alone. For myeloid cell MIS-C patient single cell RNA-seq data supplemental data with $\log_2$ fold changes directly from Lee et al. 2023 were used.[34]

Virus titer measurements

For OC43 tissue culture infection dose 50 ($TCID_{50}$) endpoint titration Vero E6/TMPRSS2 cells were seeded at 10000 cells per well in 96 F-bottom plates and incubated overnight. Supernatants containing infectious hCoV OC43 or wash control harvested post-infection were serially diluted (1:10) and added to Vero E6/TMPRSS2 cells in 8 technical replicates. Cells were incubated for 5–7 days and monitored for cytopathic effects. $TCID_{50}$/ml was calculated according to the Reed and Muench method.

For quantification of HRV16 viral titers HeLa-H1 cells were seeded in 96-well plates at a density of 20000 cells per well and incubated overnight for attachment and growth. The supernatant from infected HeLa-H1 cells transfected with OAS constructs from 5-day post-infection was collected and serially diluted in a 10-fold series using DMEM supplemented with 2% FCS. For the $TCID_{50}$ assay, 100 μL of the diluted viral supernatant series were added to fresh HeLa-H1 cells in 96-well plate after replacing the existing media and cultured at 33 °C. Cells were monitored continuously for (CPE) starting 72 hours post-infection, and $TCID_{50}$ values were calculated.

Protein synthesis assay

For the detection of protein synthesis using fluorescence microscopy, fibroblasts were seeded at 15000 cells per well on coverslips in a 24-well plate and incubated overnight at 37 °C and 5% CO_2. The next day, cells were left untreated or stimulated with IFN-α (500 IU/ml) for 23 h. Then, the Click-iT® Plus OPP Protein Synthesis Assay was performed accordingly to the manufacturer's protocol. Briefly, cells were incubated with 20 μM O-propargyl-puromycin (OPP) for 1 h before fixed with 4% PFA for 15 min at room temperature. After permeabilization for 15 min with 0.5% Triton X-100 in PBS, fluorescence labeling of the incorporated OPP was carried out by the Click-iT® reaction in the dark. After staining the DNA, cells were mounted and imaged on a Zeiss LSM980.

Proliferation assay

Growth curve analysis of fibroblasts was performed using the Incucyte Live-Cell Analysis System (Incucyte 2020B, Sartorius). Briefly, fibroblasts were seeded at 5,000 cells per 96-well and incubated for 24 h at 37 °C and 5% CO_2. Then, NucLight Rapid Red Cell Dye (1:1000) was prepared in DMEM and 100 μl was added per well. Phase-contrast and red channel images were taken every three hours, first scanning taking place at 24 h after adding the dye. Cell number was determined afterwards using the Analyze Particle plugin in ImageJ in individual images.

Please cite this article in press as: Merold et al., Structural basis for OAS2 regulation and its antiviral function, Molecular Cell (2025), https://doi.org/10.1016/j.molcel.2025.05.001

CellPress
OPEN ACCESS

RNA degradation assay

For analysis of OAS2 activity, fibroblasts and reconstituted A549 cells were stimulated with 2 μg/ml poly(I:C) high molecular weight (HMW) (InvivoGen, tlrl-pic) for 24 h. A549 *OAS2* KO cells were treated with doxycycline (1 μg/ml) for 24 h to induce OAS2 expression. Afterwards total RNA was isolated from cells using ReliaPrep™ RNA MiniPrep Systems (Promega). RNA degradation was analyzed on RNA Pico chips using Agilent Bioanalyzer 2100 (Agilent).

Immunoprecipitation and mass spectrometry

For immunoprecipitation (IP) of OAS2, 13*106 cells were seeded in 15cm dish per IP and transfected with 23.4 μg plasmid DNA using 70μl PEI (1mg/ml). Cells were harvested 24–48h post transfection and lysed in 50mM Tris-HCl pH 7.5, 150mM NaCl, 1% NP-40, 5mM EDTA supplemented with 1xcOmplete protease inhibitor for 30min on ice. After centrifugation for 30min, at 21'000 x g 4°C, cell lysates were incubated with 4μg anti-OAS2 antibody (R&D Systems, MAB1925) and 25 μl bed volume Protein G Sepharose Beads (GE Healthcare) for 2h at 4°C. Beads were centrifuged for 12'000xg, 20sec washed once with PBS and incubated either with PBS or 100mM NEM in PBS for 4h at 4°C. Beads were washed 3–5 times in PBS, 1% NP-40, 5mM EDTA followed by one wash with PBS. Sample was eluted by heating for 10min at 70 °C in 1xLithium Sample Buffer (Thermo Fisher Scientific).

In-gel trypsin digestion was performed according to standard procedures (Shevchenko et al., 2006).[138] Briefly, samples were run on a (Thermo Fisher Scientific) for about 1 cm. Subsequently, the still not size-separated single protein band per sample was cut out, reduced (50mM dithiothreitol), alkylated (55mm chloroacetamide) and digested overnight with trypsin. The peptides obtained were dried to completeness and resuspended in 0.1% formic acid prior to liquid chromatography tandem mass spectrometry (LC-MS/MS) analysis on a 42-cm column (inner diameter: 75 microns; packed with ReproSil-Pur C18-AQ 1.9-micron beads, Dr. Maisch GmbH) coupled to an Orbitrap Eclipse mass spectrometer (Thermo Fisher Scientific). Samples were measured over a 50 min linear gradient in data dependent acquisition (DDA) and positive ionization mode followed by a targeted Parallel Reaction Monitoring (PRM) measurement for selected OAS2 peptides. Raw mass spectrometry data were processed using the MaxQuant software (version 2.0.4.0) with its built-in search engine, Andromeda.[117] Spectra were searched against the UniProtKB database (Human, UP000005640, 75,777 entries downloaded on 01.2021). Enzyme specificity was set to trypsin, allowing for 2 missed cleavages, and search performed for glycine myristoylation (+210.19836) as a variable modification. Identifications were adjusted to 1% false discovery rate (FDR) at protein and peptide levels. Skyline (v.24.1)[118] was used for spectral library generation and spectrum export based on MaxQuant msms.txt output files.

Genetic investigations

The study was conducted with approval by the ethics committee of the Medical Faculty, TU Dresden, and with written informed consent by the parents of the patient.

For whole exome analysis, cDNA library preparation was done using the TWIST exome 2.0 kit (twistbioscience) and sequenced on a Next-Seq500/550 sequencer (Illumina) with an average depth of 100x. The varvis® genomics platform (varvis) was used as end to end pipeline for raw sequencing data processing, variant annotation, and variant filtering. Variants were prioritized based on clinical symptoms, allele frequency, known association with disease using publicly available databases (gnomAD, OMIM, HGMD, ClinVar, etc.), and in silico predictions regarding functional effects.

For segregation analysis, the identified *OAS2* variant (c.1572C>G, p.(Phe524Leu), NM_002535.3) was sequenced by dideoxy sequencing on an ABI 3730XL genetic analyzer (ThermoFischer) using the following primers: OAS2_s 5′-gagatgctccctgtgtcttaga-3′; OAS2_as 5′-ccccatggtcagaacaaagac-3′.

Sanger sequencing

Genomic DNA was extracted from blood using the QIAamp DNA Blood Mini Kit (Qiagen). Genomic DNA flanking the *OAS2* (ENST00000392583_7) mutation was amplified by polymerase chain reaction (PCR) using gene-specific primers [Eurofins MWG Operon; OAS2-for: GAGATGCTCCCTGTGTCTTAGA and OAS2-rev: CCCCATGGTCAGAACAAAGAC] and sequenced in both directions using the service from Eurofins Genomics. Data were analyzed using the Snapgene software.

QUANTIFICATION AND STATISTICAL ANALYSIS

Statistical significance was calculated as indicated in Figure Legends and represented as ns $p \leq 0.05$, * $p \leq 0.05$, ** $p \leq 0.01$, *** $p \leq 0.001$, and **** $p \leq 0.0001$ using GraphPad Prism 10.3.1. and RStudio 2024.09.1 + 394. *n* indicates number of independent repeats/biological replicates.

For quantification of OAS2 colocalization with ER and Golgi markers and dsRNA, colocalization analysis was conducted with the Huygens Professional 19.10 software, employing the "Huygens Colocalization Analyzer" and the Costes method to calculate Pearson correlation coefficients.

For quantification of OAS2 levels in patient and WT fibroblasts (two different donors), mean fluorescence intensity (MFI) was quantified using ImageJ v1.54k.